日本磁気学会
ISSN 2432-0250
Journal of the Magnetics Society of Japan
Electronic Journal URL: https://www.jstage.jst.go.jp/browse/msjmag

Vol.48 No.2　2024

Journal

JOURNAL OF THE MAGNETICS SOCIETY OF JAPAN

Vol.48 No.2 2024

日本磁気学会

ISSN 2432-0250

HP: http://www.magnetics.jp/ e-mail: msj@bj.wakwak.com

Electronic Journal: http://www.jstage.jst.go.jp/browse/msjmag

永久磁石の熱磁気特性測定に使用される装置一覧

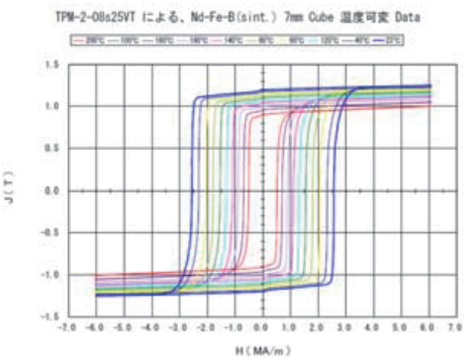

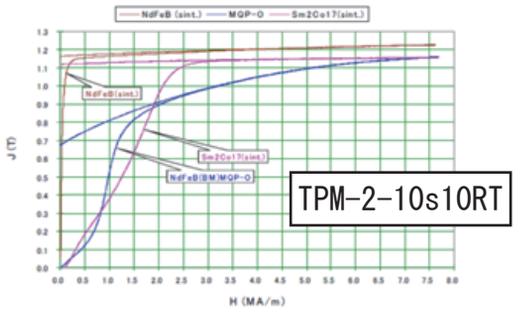

TPM-2-10s10RT

全自動温度可変型 パルス励磁式 B-H トレーサ（～200℃）

TPM-2-08s25VT

磁石用 磁束温度係数測定 及び
可逆 / 不可逆減磁温度 測定装置
TDF-5-300auto（室温～300℃）

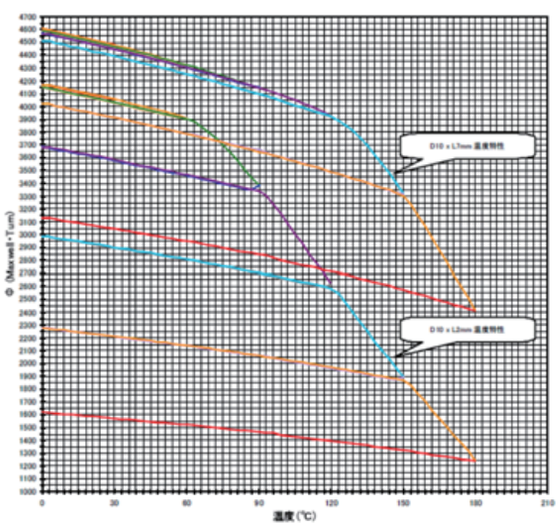

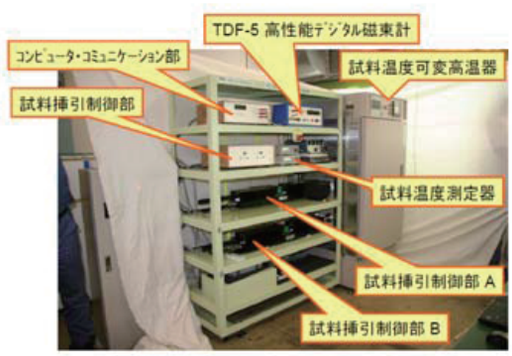

高温 B-H 特性測定装置 TRF-5BH-25auto（～250℃）

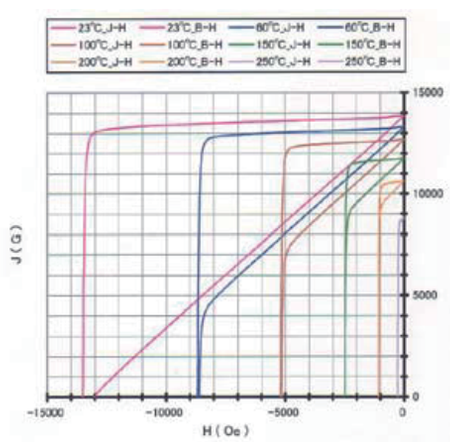

TOEI 東英工業株式会社 Tel: 042-791-1211
〒194-0035 東京都町田市忠生 1-8-13 http://www.toeikogyo.co.jp

Journal of the Magnetics Society of Japan
Vol. 48, No. 2

Electronic Journal URL: https://www.jstage.jst.go.jp/browse/msjmag

CONTENTS

J. Magn. Soc. Jpn., **48**, 17-20 (2024) <Paper>

Enhancement of coercivity for $Sm(Fe\text{-}Co)_{12}$-B thin films by introduction of Sm seed layer

Y. Mori†, S. Nakatsuka, S. Hatanaka, M. Doi, and T. Shima
Graduate School of Engineering, Tohoku Gakuin Univ., *Shimizukoji , Sendai 984-8588, Japan*

To improve the coercivity of $Sm(Fe\text{-}Co)_{12}$-B thin film, a Sm seed layer was introduced between a V buffer layer and a $Sm(Fe\text{-}Co)_{12}$-B layer, and the thickness of the $Sm(Fe\text{-}Co)_{12}$-B layer was varied. From the result of XRD patterns measured in an out-of-plane configuration, peaks from (002) and (004) of the $ThMn_{12}$-type crystal structure were observed for all samples. The intensity of these peaks was reduced by decreasing the thickness of the $Sm(Fe\text{-}Co)_{12}$-B layer; however, it was recovered by introducing a Sm seed layer. Although the coercivity was decreased due to the reduction in the thickness of the $Sm(Fe\text{-}Co)_{12}$-B layer, a large coercivity of 1.87 T was obtained in an Al-diffused thin film, which was thinned to 50 nm while introducing a Sm seed layer.

Keywords: coercivity, $ThMn_{12}$ compound, $Sm(Fe\text{-}Co)_{12}$-B film, grain boundary diffusion, seed layer

1. Introduction

RFe_{12} (R: rare earth element) compounds with a tetragonal $ThMn_{12}$-type crystal structure are candidates for new high-performance permanent magnetic materials because of their high saturation magnetization due to a composition with a high Fe content. $SmFe_{12}$-based compounds possess superior intrinsic magnetic properties compared with $Nd_2Fe_{14}B$ sintered magnets at room and elevated temperatures[1)-7)]. For example, saturation magnetization ($\mu_0 M_s$ = 1.78 T), a high anisotropy field ($\mu_0 H_A$ = 12 T) at room temperature, and a high Curie temperature (T_C = 879 K) have been realized for $Sm(Fe_{0.8}Co_{0.2})_{12}$ thin film deposited on a MgO single crystal substrate with a V buffer layer[2)]. However, stabilizing elements such as Al, Si, Ti, V, Co, W, and Zr must be substituted with a part of Fe sites since RFe_{12} compounds are well known to exhibit thermo-dynamical instability in bulk form[8)-10)].

Recently, Sepehri-Amin et al. reported that the achievement of a high coercivity of 1.2 T and formation of a columnar structure in which anisotropic $SmFe_{12}$ grains are enveloped by an amorphous grain boundary phase with a width of 2 ~ 3 nm were successfully realized for $Sm(Fe_{0.8}Co_{0.2})_{12}B_{0.5}$ thin film[11),12)]; however, the value of the coercivity was about 10% of the anisotropy field of $Sm(Fe_{0.8}Co_{0.2})_{12}$ thin film. Dempsey et al. reported that a coercivity of 2.8 T, which is 37% of the anisotropy field of the $Nd_2Fe_{14}B$ phase, was obtained for Nd-Fe-B thick film[13)]. The main difference in microstructure between Nd-Fe-B thick film and $Sm(Fe_{0.8}Co_{0.2})_{12}B_{0.5}$ thin film is the composition of the grain boundaries[6)], and the grain boundary phase of $Sm(Fe_{0.8}Co_{0.2})_{12}B_{0.5}$ has a large Fe composition (72 at.%) that is higher than Nd-Fe-B thick film (60 at.%)[6)]; thus, further improvement to the coercivity of $Sm(Fe_{0.8}Co_{0.2})_{12}B_{0.5}$ thin film was suggested by reducing the Fe content in the grain boundary phase[6)].

Corresponding author: Y. Mori
(e-mail: s236532001@g.tohoku-gakuin.ac.jp).

Grain boundary diffusion using non-magnetic elements is expected to improve magnetic properties, and many achievements have been made to improve these properties[14)~17)]. For example, Bolyachkin et al. reported that the coercivity was increased by infiltration of a Si cap layer into the grain boundary phase of $Sm(Fe_{0.8}Co_{0.2})_{12}B_{0.5}$ (100 nm) thin film[16)]. Then, microstructural observation by cross-sectional STEM-EDS revealed that the penetration depth of the diffused Si was found in a region approximately 25 nm from the top surface of the $Sm(Fe_{0.8}Co_{0.2})_{12}B_{0.5}$ layer[16)]. In addition, micromagnetic simulation based on the results of microstructural observation and magnetic properties predicts that a coercivity of 1.9 T will be obtained when diffused Si reaches 90 nm below the top surface of the $Sm(Fe_{0.8}Co_{0.2})_{12}B_{0.5}$ layer; furthermore, if the formation of soft magnetic phases such as α-Fe or α-(Fe-Co) existing in the initial interface between the V buffer layer and the $Sm(Fe_{0.8}Co_{0.2})_{12}B_{0.5}$ layer are suppressed completely, the coercivity will be enhanced to approximately 6.0 T[16)]. Thus, to obtain a large coercivity in $Sm(Fe\text{-}Co)_{12}B$ thin films, it is necessary to sufficiently diffuse non-magnetic elements into the grain boundary phase while controlling the microstructure at the bottom of the $Sm(Fe\text{-}Co)_{12}B$ layer. Recently, we reported that the formation of an α-Fe phase can be suppressed while maintaining a high coercivity by introducing a Sm seed layer between the V buffer layer and the $Sm(Fe\text{-}Co)_{12}$-B layer[19)]. In this study, to improve the coercivity of $Sm(Fe\text{-}Co)_{12}$-B thin film, a Sm seed layer was introduced into $Sm(Fe\text{-}Co)_{12}$-B thin films with the diffusion of a Si or Al cap layer. Furthermore, the thickness of the $Sm(Fe\text{-}Co)_{12}$-B thin films was varied. Their magnetic properties and crystal structures were investigated in detail.

2. Experimental procedure

The samples were prepared by using an ultra-high vacuum magnetron sputtering system with a base pressure of less than 4.0×10^{-7} Pa. First, a V buffer layer of 20 nm and a Sm seed layer of 2 nm were

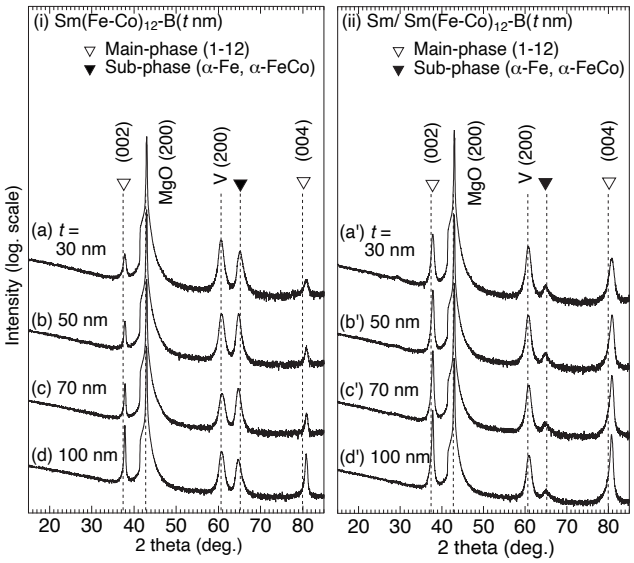

Fig. 1. XRD patterns for $Sm(Fe\text{-}Co)_{12}$-B thin films with different thicknesses of magnetic layer (t) between 30 and 100 nm. (i) denotes samples without Sm seed layer, while (ii) shows those where Sm seed layer has thickness of 2 nm.

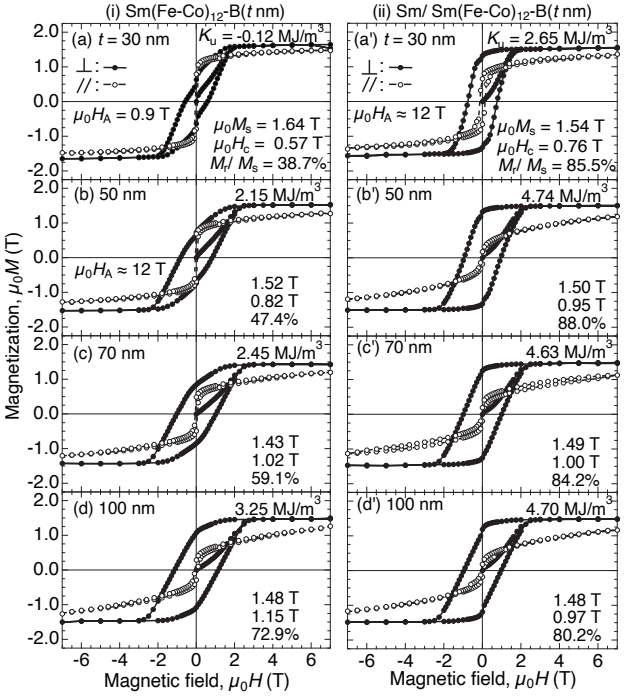

Fig. 2. Magnetization curves for $Sm(Fe\text{-}Co)_{12}$-B thin films with different thicknesses of magnetic layer. Filled and open circles denote curves measured in perpendicular and parallel directions to film plane, respectively.

deposited onto a MgO (100) single crystal substrate at a substrate temperature T_s of 400°C. Then, a $Sm(Fe\text{-}Co)_{12}$-B layer of t nm was deposited by co-sputtering with Sm, Fe, $Fe_{50}Co_{50}$ and $Fe_{80}B_{20}$ targets, and t was changed to 30, 50, 70, and 100 nm. Film compositions at each film thickness were determined to be $Sm_{5.4}Fe_{74.2}Co_{18.6}B_x$ (at.%) (t = 30 nm), $Sm_{6.9}Fe_{73.9}Co_{19.2}B_x$ (t = 50 nm), $Sm_{7.4}Fe_{73.7}Co_{18.9}B_x$ (t = 70 nm), and $Sm_{7.2}Fe_{74.2}Co_{18.6}B_x$ (t = 100 nm) by energy dispersive X-ray analysis (EDX). However, it is noted that due to the detection limit of light elements, the composition of B cannot be determined by EDX. Subsequently, an Al cap layer of 35 nm and a Si cap layer of 8 nm were deposited at a T_s of 400°C onto the $Sm(Fe\text{-}Co)_{12}$-B layer, and sufficient post-annealing was performed to fully diffuse the cap layer materials. The annealing temperature was set to 400°C for 4 hours (Al-diffused film), and additional post annealing was not performed on the Si-diffused film. Finally, a V layer with a thickness of 10 nm was deposited as a protective layer to prevent oxidation. The crystal structures were analyzed by X-ray diffraction (XRD) with Cu-K_α radiation employing an out-of-plane configuration. The magnetic properties were evaluated by using a superconducting quantum interference device (SQUID) magnetometer. All measurements were performed at room temperature.

3. Results and discussion

X-ray diffraction patterns for $Sm(Fe\text{-}Co)_{12}$-B (t nm) and Sm(2 nm)/$Sm(Fe\text{-}Co)_{12}$-B(t nm) thin films with different thicknesses for the magnetic layer (t) are shown in Fig. 1. Peaks from (002) and (004) for the $ThMn_{12}$-type crystal structure are clearly observed for all samples. Note that the peak position shown by the broken line represents the literature value of the $SmFe_{12}$ compound without B addition[2], and it has already been reported that the peak position is shifted to the high angle side by co-deposition with B[12]. The intensities of the (002) and (004) peaks were reduced by decreasing the thickness of the magnetic layer for the sample without a Sm seed layer. However, it was confirmed that by introducing the Sm seed layer, the (002) and (004) peaks could be clearly observed, and the intensity of the peak around 65° corresponding to an α-Fe phase was remarkably reduced. These results indicated that the introduction of the Sm seed layer improved the crystal orientation and suppressed the formation of the α-Fe phase. It has already been reported that a Fe-V(Co) phase was formed at the interface between the Sm(Fe-Co) layer and the V buffer layer[5]. Therefore, it is thought that inserting the Sm seed layer at the interface suppressed the formation of the α-Fe(-Co) phase.

Magnetization curves for $Sm(Fe\text{-}Co)_{12}$-B (t nm) and Sm(2 nm)/$Sm(Fe\text{-}Co)_{12}$-B(t nm) thin films with different thicknesses for the magnetic layer are shown in Fig. 2. The filled and open circles denote the curves measured in perpendicular and parallel directions to the film plane, respectively. In the samples without the Sm seed layer, μ_0H_c, the uniaxial magnetic anisotropy (K_u) and squareness (M_r/M_s) were increased by increasing t, and it was confirmed that the direction of the easy magnetization changed from in-plane to perpendicular as the film thickness increased. A high μ_0M_s of 1.48 T, high μ_0H_c of 1.15 T, high M_r/M_s of 72.9%, and moderate K_u of 3.25 MJ/cm^3 were obtained for the film with t = 100 nm. On the other hand, when the Sm seed layer was introduced, perpendicular magnetic anisotropy was confirmed even at t = 30 nm, and a μ_0H_c of

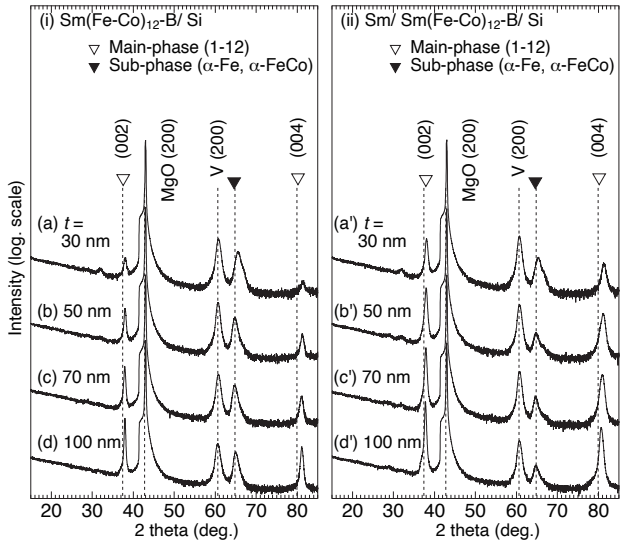

Fig. 3. XRD patterns for Sm(Fe-Co)$_{12}$-B/Si thin films with different thicknesses of magnetic layer (t) between 30 and 100 nm. Thickness of Si cap layer was fixed at 8 nm.

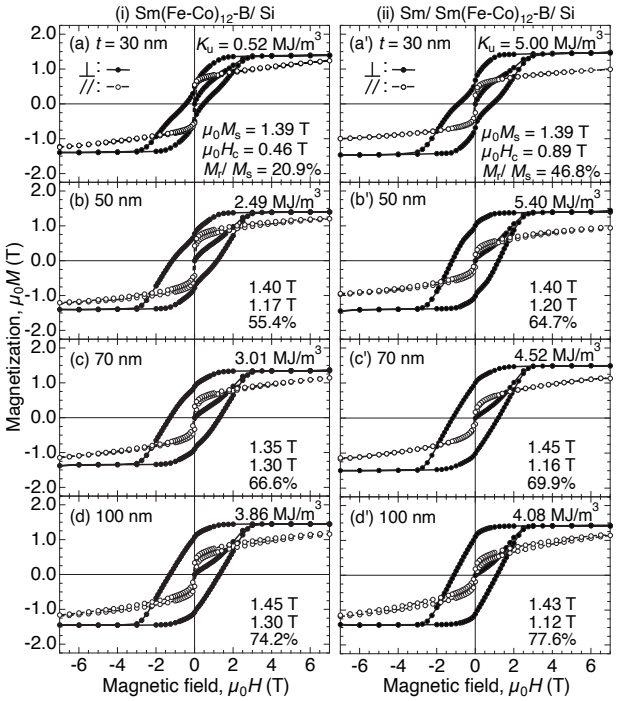

Fig. 4. Magnetization curves for Sm(Fe-Co)$_{12}$-B/Si thin films with different thicknesses of magnetic layer (t).

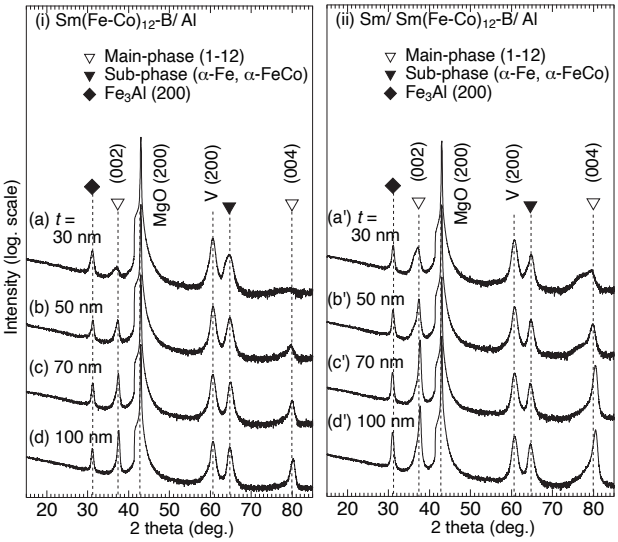

Fig. 5. XRD patterns for Sm(Fe-Co)$_{12}$-B/ Al thin films with different thicknesses of magnetic layer (t). Thickness of Al cap layer was fixed at 35 nm.

approximately 1 T and high K_u of 4.7 MJ/cm^3 were obtained above t = 50 nm. Therefore, it was confirmed that the introduction of the Sm seed layer plays an important role in improving the magnetic properties and crystallographic orientation of the 1:12 phase.

To improve $\mu_0 H_c$, diffusion of a Si and Al cap layer followed by appropriate post-annealing were performed. XRD patterns for (i) Sm(Fe-Co)$_{12}$-B(t nm)/Si (8 nm) and (ii) Sm(2 nm)/Sm(Fe-Co)$_{12}$-B(t nm)/Si(8 nm) thin films with different t are shown in Fig. 3. The intensity of the peaks from the 1:12 phase was increased remarkably by introducing the Sm seed layer. Also, in the case of the film with t = 30 nm, the peak position of the α-Fe phase was slightly shifted to a higher angle, suggesting that the Si that diffused into the Sm(Fe-Co)$_{12}$-B layer reached the bottom.

Magnetization curves for (i) Sm(Fe-Co)$_{12}$-B(t nm)/Si(8 nm) and (ii) Sm(2nm)/Sm(Fe-Co)$_{12}$-B(t nm)/Si(8 nm) thin films with different t are shown in Fig. 4. It was confirmed that $\mu_0 H_c$ was increased by increasing t for the films without a Sm seed layer, and a high $\mu_0 H_c$ of 1.30 T was obtained for the film with t = 100 nm. However, when the Sm seed layer was introduced, the $\mu_0 H_c$ was increased for the films with t = 30 and 50 nm, but the $\mu_0 H_c$ of the films with t = 70 and 100 nm was decreased. Furthermore, in the film with the Sm seed layer introduced, $\mu_0 H_c$ changed from increasing to decreasing as the film thickness increased.

XRD patterns for Al-diffused Sm(Fe-Co)$_{12}$-B thin films with and without a Sm seed layer are shown in Fig. 5. t was changed between 30 and 100 nm, while the thickness of the Al cap layer was fixed at 35 nm. Remarkable peaks from (002) and (004) from the 1:12 phase began to be observed above t = 50 nm, and their intensity was increased by increasing t for the film without the Sm seed layer. In addition, it was confirmed that the (002) and (004) peak position in the Al-diffused films were shifted to a lower angle compared with the Si-diffused film (Fig. 3). This is considered to be due to the interstitial diffusion of Al element into the 1:12 phase, increasing the lattice spacing. Furthermore, as the film thickness increased, their peak positions shifted to a higher angle, which is thought to be due to the fact that the amount of diffusion in the Al element from the cap layer decreased with the increase in film thickness.

Magnetization curves for Al-diffused Sm(Fe-Co)$_{12}$-B thin films with and without a Sm seed layer are shown in Fig. 6. Magnetic properties such as a $\mu_0 M_s$ of 1.17 T, high $\mu_0 H_c$ of 1.78 T, M_r/M_s of 69.0%, and K_u of 3.88 MJ/cm^3 were obtained for the Sm(Fe-Co)$_{12}$-B(100 nm)/Al(35 nm) thin film. The coercivity was decreased

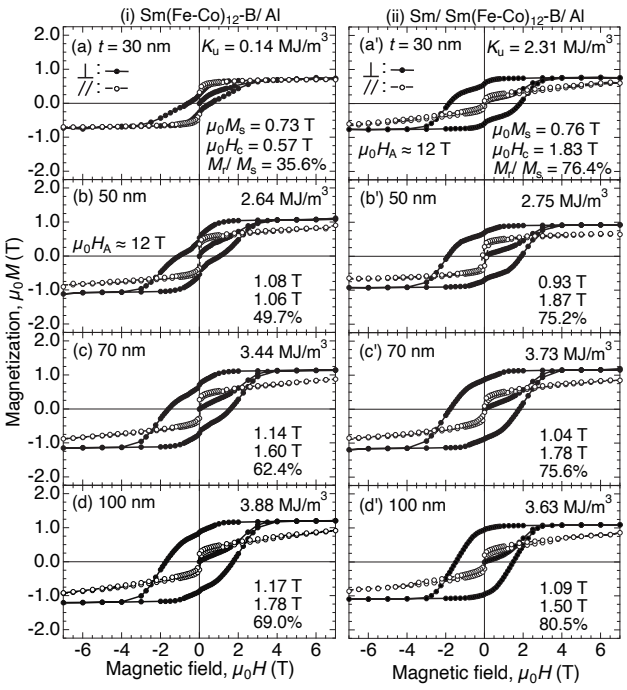

Fig. 6. Magnetization curves for Sm(Fe-Co)-B (t nm)/Al (35 nm) thin films with and without Sm seed layer. t was changed from 30 to 100 nm.

to 1.50 T by the introduction of the Sm seed layer. However, the highest $\mu_0 H_c$ of 1.87 T was obtained for the Sm/Sm(Fe-Co)$_{12}$-B/Al thin film with t = 50 nm. The penetration depth of Al diffusion into Sm(Fe-Co)$_{12}$-B (100 nm)/Al (35 nm) was reported to be about 50 nm[20]. Hence, the enhancement in $\mu_0 H_c$ is thought to be due to the increase in the volume ratio of an Al-diffused grain boundary phase in the Sm(Fe-Co)$_{12}$-B layer. However, there was a kink where the hysteresis loops were measured in the perpendicular direction at near zero magnetic field. This can be attributed to the formation of a ferromagnetic Fe_3Al compound present in the region of the Al cap layer or the Al-diffused grain boundary phase.

4. Conclusion

The effects of introducing a Sm seed layer between a V buffer layer and a Sm(Fe-Co)$_{12}$-B layer on crystal structures and magnetic properties for Sm(Fe-Co)-B, Sm(Fe-Co)$_{12}$-B/Si, and Sm(Fe-Co)$_{12}$-B/Al thin films were investigated in detail. Since $\mu_0 H_c$ was increased to 1.30 T (Si diffusion) and 1.78 T (Al diffusion) at t = 100 nm, each cap layer material is thought to have infiltrated into the grain boundary phase in the Sm(Fe-Co)$_{12}$-B layer. Magnetic properties such as $\mu_0 H_c$, M_r/M_s, and K_u and the intensities of (002) and (004) peaks for the 1:12 phase of the Sm(Fe-Co)$_{12}$-B thin film were decreased by decreasing t. However, the $\mu_0 H_c$ of Sm/Sm(Fe-Co)$_{12}$-B/Si and Sm/Sm(Fe-Co)$_{12}$-B/Al thin films held a maximum value at t = 50 nm, and the highest $\mu_0 H_c$ of 1.87 T was obtained for Sm(Fe-Co)$_{12}$-B/Al thin film with a Sm(2 nm) seed layer. The enhancement of $\mu_0 H_c$ was considered to be due to the increment of the volume ratio of the Al-diffused grain boundary phase in the Sm(Fe-Co)$_{12}$-B layer, and it is considered that the result of diffusion/infiltration in the grain boundary phase can pave the way to realizing applications of Sm(Fe-Co)$_{12}$-based permanent magnets.

Acknowledgements This work was performed at the Research Institute for Engineering and Technology (High-Tech Research Center) at Tohoku Gakuin University. This work was partially supported by MEXT Program: Data Creation and Utilization-Type Material Research and Development Project (Digital Transformation Initiative Center for Magnetic Materials) Grant Number JPMXP1122715503.

References

1) B. Fuquan, J. L. Wang, O. Tegus, W. Dagula, N. Tang, F. M. Yang, G. H. Wu, E. Brück, F. R. de Boer and K. H. J. Buschow: *J. Magn. Magn. Mater.*, **290**, 1192 (2005).
2) Y. Hirayama, Y. K. Takahashi, S. Hirosawa and K. Hono: *Scr. Mater.*, **138**, 62 (2017).
3) A. M. Gabay and G. C. Hadjipanayis: *Scr. Mater.*, **154**, 284 (2018).
4) P. Tozman, H. Sepehri-Amin, Y. K. Takahashi and K. Hono: *Acta Mater.*, **153**, 354 (2018).
5) P. Tozman, Y. K. Takahashi, H. Sepehri-Amin, D. Ogawa, S. Hirosawa and K. Hono: *Acta Mater.*, **178**, 114 (2019).
6) Y. K. Takahashi, H. Sepehri-Amin and T. Ohkubo: *Adv. Mater.*, **22**, 449 (2021).
7) P. Tozman, H. Sepehri-Amin and K. Hono: *Scr. Mater.*, **194**, 113686 (2021).
8) X. C. Kou, T. S. Zhao, R. Grössinger, H. R. Kirchmayr, X. Li and F. R. de Boer: *Phys. Rev. B*, **47**, 3231 (1993).
9) M. Artigas, C. Piquer, J. Rubin and J. Bartolome: *J. Magn. Magn. Mater.*, **196**, 653 (1999).
10) I. Dirba, J. Li, H. Sepehri-Amin, T. Ohkubo, T. Schrefl and K. Hono: *J. Alloys Compd.*, **804**, 155 (2019).
11) H. Sepehri-Amin, Y. Tamazawa, M. Kambayashi, G. Saito, Y. K. Takahashi D. Ogawa, T. Ohkubo, S. Hirosawa, M. Doi, T. Shima and K. Hono: *Acta Mater.*, **194**, 337 (2020).
12) M. Kambayashi, H. Kato, Y. Mori, M. Doi and T. Shima: *J. Magn. Soc. Jpn.*, **45**, 66 (2021).
13) N. M. Dempsey, T. G. Woodcock, H. Sepehri-Amin, Y. Zhang, H. Kennedy, D. Givord, K. Hono and O. Gutfleisch: *Acta Mater.*, **61**, 4920 (2013).
14) A. K. Srinithi, H. Sepehri-Amin, X. Tang, P. Tozman, J. Li, J. Zhang, S. Kobayashi, T. Ohkubo, T. Nakamura and K. Hono: *J. Magn. Magn. Mater.*, **529**, 167866 (2021).
15) D. Ogawa, X. Xu, Y. K. Takahashi, T. Ohkubo, S. Hirosawa and K. Hono: *Scr. Mater.*, **164**, 140 (2019).
16) A. Bolyachkin, H. Sepehri-Amin, M. Kanbayashi, Y. Mori, T. Ohkubo, Y. K. Takahashi, T. Shima and K. Hono: *Acta Mater.*, **227**, 117716 (2022).
17) Y. Mori, S. Hatanaka, M. Kambayashi, S. Nakatsuka, K. Hirayama, M. Doi and T. Shima: *J. Magn. Soc. Jpn.*, **47**, 103 (2023).
18) A. K. Srinithi, Xin Tang, H. Sepehri-Amin, J. Zhang, T. Ohkubo and K. Hono: *Acta Mater.*, **256**, 119111 (2023).
19) S. Nakatsuka, Y. Mori, S. Hatanaka, M.Doi and T. Shima: *Digest book "IEEE International Magnetics Conference," Intermag 2023*, Sendai Japan, May 2023, p. 212 (2023).

Received Oct. 30, 2023; Accepted Dec. 12, 2023

J. Magn. Soc. Jpn., **48**, 21-27 (2024) <Paper>

Microwave Transmission Theory for On-Chip Ultrastrong-Coupled Magnon-Polariton in Dynamical Inductors

Takahiro Chiba[1,2], Takashi Komine[3], and Tomosuke Aono[3]

[1]Frontier Research Institute for Interdisciplinary Sciences (FRIS), Tohoku Univ., *Sendai, Miyagi 980- 8578, Japan*
[2]Department of Applied Physics, Graduate School of Engineering, Tohoku Univ., *Sendai, Miyagi 980-8579, Japan*
[3]Graduate School of Science and Engineering, Ibaraki Univ., *Hitachi, Ibaraki, 316-8511, Japan*

We present a microwave transmission theory for recently proposed ultrastrong-coupled magnon-polariton (MP) in dynamical inductors which consist of a coil involving a magnetic insulator. Combining with the *RLC*-circuit and Landau-Lifshitz-Gilbert equations, we formulate the electric impedance of MP as a coupled oscillator under the corresponding principle. Based on the transmission (*ABCD* or *F*) matrix approach, we further calculate S_{21} being a scattering parameter for the microwave transmission measurement passing through an *RLC*-circuit with the dynamical inductor. By tunning the size of the dynamical inductor, we theoretically demonstrate an on-chip ultrastrong-coupled MP at room temperature, which reaches a coupling ratio about 0.55 and cooperativity about 2×10^5 with material parameters of $Y_3Fe_5O_{12}$. This work paves the way for quasi-two-dimensional circuit/wave-guide based magnonics for quantum information technology.

Keywords: hybrid quantum systems, magnons, polaritons, magnetic insulators, ferromagnetic resonance, microwave techniques, quantum information technology

1. Introduction

A strong microwave-magnet interaction gives rise to a hybrid quantum system with energy levels distinct from those of the microwave (photon) or the magnet (magnon), namely, magnon-polariton (MP) with a level repulsion characterized by Rabi-like energy splitting.[1)] In such a "strong coupling" regime, quantum information can be easily transferred from the microwave to the magnet and vice versa, whose feature is useful in quantum information technologies, such as magnon-based sensors,[2)] memories,[3,4)] transducers,[5,6)] and masers.[7)] However, without a few exceptions utilizing planar resonators,[8-11)] most experiments have so far focused on strong coupling for cavity magnonic systems based on three-dimensional microwave cavities with several-tens millimeters scales.[12–15)] For practical applications based on solid-state devices, a realization of on-chip MPs at room temperature is highly desired.

Recently, quantum magnonic systems with on-chip superconducting/ferromagnetic multilayers have achieved ultrastrong coupling (USC) with the coupling ratio $g/\omega_r \approx 0.6$ below several Kelvins,[16,17)] where g denotes the coupling strength and ω_r is the transition (resonance) angular frequency of the system. The USC (defined for $g/\omega_r \geq 0.1$) could enhance the performance of quantum devices, e.g., enabling fast transfer of quantum information before decoherence of quantum states. Furthermore, in the USC regime, the breakdown of the standard quantum-optical approximation (the rotating-wave approximation, RWA) allows eigenstates to combine higher/lower states with different particle numbers, which produces exotic quantum effects.[18)]

Very recently, an ultrastrong-coupled MP with $g/\omega_r \approx 0.28$ has been demonstrated at room temperature by a theory that utilizes a dynamical inductor consisting of a small coil involving a magnetic insulator (MI) in an *RLC*-circuit.[19)] The microwave-magnet interaction, which is govern by the magnetic-dipole (Zeeman) interaction, i.e. the inner product of the microwave magnetic field and magnetization of the magnet, is enhanced by the coil that aligns the microwave magnetic field and generates strong overlap among the magnon-photon. In order to generate a coherent magnon-photon coupling (magnetic-dipole interaction) inside the coil, the magnetization of MI is required to be normal to the microwave magnetic field, so that in the previous work[19)] an interfacial magnetic anisotropy induced by a topological insulator contact[20–22)] and an external static magnetic field normal to the microwave field have been utilized. It is worth to note that an in-plane static magnetic field normal to the microwave field also could drive the ultrastrong-coupled MP.

Towards the experimental realization of the proposed room temperature ultrastrong-coupled MP, the above setup could be generalized to other potential magnonic systems. An alternative is strain-induced interfacial magnetic anisotropy in garnet thin films on a controlled substrate, such as $Y_3Fe_5O_{12}$ (YIG)/$Gd_3Ga_5O_{12}$ (GGG)[21)] and Bi-doped YIG/GGG.[24)] Also, two-dimensional van der Waals magnets with a strong perpendicular magnetic anisotropy[25)] may be potential candidates. Thus, the ultrastrong-coupled MP in the dynamical inductor could be ubiquitous for a number of magnonic systems. On the other hand, the previous work[19)] has presented a theoretical model of an ultrastrong-coupled MP in the dynamical inductor by treating the *RLC*-circuit as an

Corresponding author:
Takahiro Chiba (e-mail: takahiro.chiba.e2@tohoku.ac.jp).

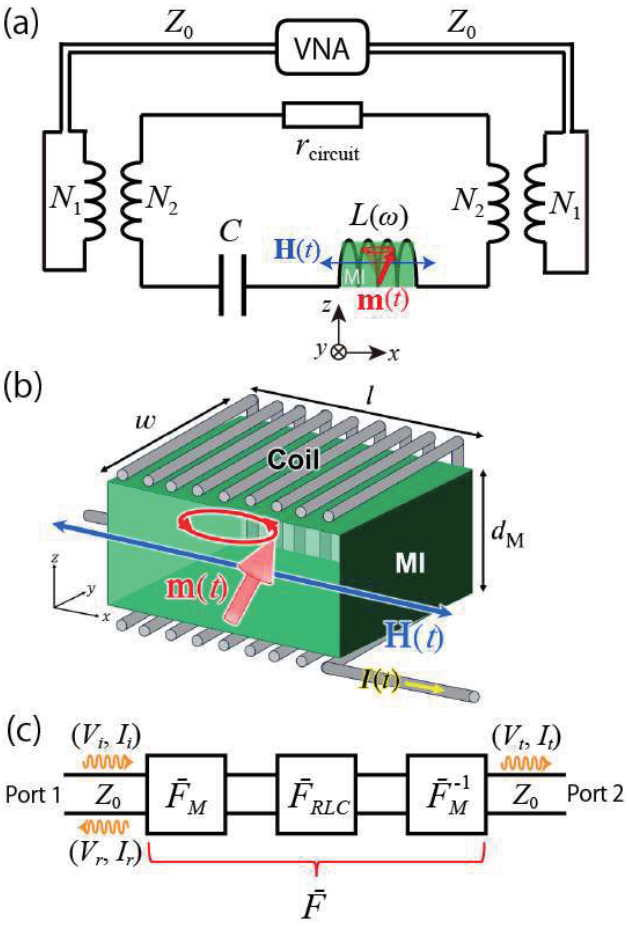

Fig. 1 (a) Schematics of a two-port microwave network with a *RLC*-circuit that consists of a dynamical inductor $L(\omega)$ and a capacitor C, in which r_{circuit} is the resistance due to leads and electrodes, the parameter N_1/N_2 indicates the inductive coupling between the port and the *RLC*-circuit, and Z_0 represents the impedance of the microwave feedline. Also, VNA denotes the vector network analyzer. The dynamical inductor consists of a magnetic insulator (MI) embedded within a coil. The red arrow is the precessional magnetization directions $\mathbf{m}(t)$ at the resonance driven by a microwave magnetic field $\mathbf{H}(t)$ due to alternating current $I(t)$.
(b) Schematic structure of the dynamical inductor that consists of a coil involving a MI thin film with thickness d_{M}. The coil is assumed to be wound around the thin film of MI.
(c) Corresponding cascade connection of two-port networks characterized by the transmission (*ABCD* or *F*) matrix. (V_i, I_i), (V_r, I_r), and (V_t, I_t) are microwave power vectors for incident, reflection, and transmission waves, respectively.

electric admittance. This formulated observable (admittance) is inconvenient for standard microwave transmission measurements, which measure a scattering parameter S_{21} in a two-port network by using the vector network analyzer (VNA). Therefore, from the viewpoint of the experiment, it is desirable to model the scattering parameter based on the microwave circuit theory.

In this paper, we develop the theory of recently proposed ultrastrong-coupled MP in dynamical inductors by taking into consideration of a practical two-port microwave network. Combining with the *RLC*-circuit and Landau-Lifshitz-Gilbert (LLG) equations, we formulate the electric impedance of MP as a coupled oscillator under the corresponding principle. We further calculate S_{21} for the microwave transmission passing through an *RLC*-circuit with the dynamical inductor using the transmission (*ABCD* or *F*) matrix approach. By tuning the size of the dynamical inductor, we theoretically demonstrate an on-chip ultrastrong-coupled MP with realistic material parameters at room temperature. In addition, we discuss a way to achieve the deep-strong coupled MP in the dynamical inductor.

2. Theoretical Model

2.1 Coupled magnon-photon oscillator

Here, we describe a MP as a coupled magnon-photon oscillator under the corresponding principle.[1,19] The system is schematically shown in Fig. 1 (a) as a two-port microwave network with an *RLC*-circuit, in which the perpendicular magnetization of the inserted MI, which is stabilized by an external static magnetic field, is excited by the microwave magnetic field $\mathbf{H}(t)$ with a resonant mode of the *RLC*-circuit. The circuit mode is coupled to the Kittel mode of magnetization dynamics $\mathbf{m}(t)$ with zero magnon wavenumber via the magnetic-dipole (Zeeman) interaction that is responsible for the coherent magnon-photon coupling.

Inside the coil inserted MI, the magnetization dynamics is described by the LLG equation

$$\frac{d\mathbf{m}}{dt} = -\gamma\mathbf{m}\times\left(-\frac{1}{M_{\text{s}}}\frac{\delta U_{\text{m}}}{\delta\mathbf{m}} + \mu_0\mathbf{H}(t)\right) + \alpha\mathbf{m}\times\frac{d\mathbf{m}}{dt} \quad (1)$$

where $\mathbf{m}(=\mathbf{m}(t))$ is the unit vector along the magnetization direction of MI with the saturation magnetization M_{s}, γ is the gyromagnetic ratio, μ_0 is the permeability of free space, and α is the intrinsic Gilbert damping constant. Here, the total magnetic energy is assumed by

$$U_{\text{m}} = -\mu_0 M_{\text{s}}\mathbf{m}\cdot\mathbf{H}_0 + \mu_0 M_{\text{s}}^2 m_z^2/2 + K_u\left(1-m_z^2\right) \quad (2)$$

where $\mathbf{H}_0 = H_0\hat{\mathbf{z}}$ is the external static magnetic field for the perpendicular magnetization configuration and K_u is uniaxial magnetic anisotropy energy. Note that the second term in Eq. (2) describes the demagnetization field for a thin film of MI. Also, $\mathbf{H}(t)\approx nI(t)\hat{\mathbf{x}}$ is the microwave magnetic field induced by an alternating current $I(t)$ via Ampère's law inside the coil with a turn number density n, which is governed by the *RLC*-circuit equation (Kirchhoff's voltage law)

$$\frac{Q(t)}{C} + r_{\mathrm{circuit}} I(t) + \frac{d\Phi(t)}{dt} = V(t) \tag{3}$$

where $Q(t)$ is the accumulated charge on the capacitor with an electrostatic capacitance C, r_{circuit} represents the resistance due to leads and electrodes in the RLC-circuit, and $V(t) = V_0 e^{-i\omega t}$ is an applied ac voltage with an angular frequency ω (experimentally due to input signal from the VNA). Here, for $\mathbf{H}(t)$-linear magnetization dynamics: $\mathbf{m}(t) = (\delta m_x(t), \delta m_y(t), 1) \propto \mathbf{H}(t)$ with $|\delta m_x|, |\delta m_y| \ll 1$, the magnetic flux in the dynamical inductor is given by

$$\Phi(t) = L_0 I(t) + L_0 M_s (\mathbf{m} \cdot \hat{\mathbf{x}})/n \approx L(\omega) I(t) \tag{4}$$

where $L_0 \equiv L(\omega = 0) = \mu_0 n^2 lwd$ is a static (bare) inductance with the length l, width w, and thickness d (See Fig. 1 (b) for the coil geometry). Note that the coil is assumed to be wound around a thin film of MI with the thickness $d_{\mathrm{M}} \approx d$. In Eq. (4), the term $L_0 M_s (\mathbf{m} \cdot \hat{\mathbf{x}})/n$ induces a voltage in the RLC-circuit via Faraday's law.

By combining the RLC-circuit and LLG equations for the circuit current $I(t) = dQ/dt = I_0 e^{-i\omega t}$ and the linearized dynamical magnetization $m_\perp = \delta m_x - i\delta m_y$ with a harmonic time dependence $e^{-i\omega t}$, respectively, we get an eigenvalue equation for a coupled magnon-photon oscillator:

$$\bar{\Omega}(\omega) \begin{pmatrix} I_0 \\ M_s m_\perp \end{pmatrix} = \begin{pmatrix} i\omega V_0/L_0 \\ 0 \end{pmatrix} \tag{5}$$

with

$$\bar{\Omega}(\omega) = \begin{pmatrix} \omega^2 - \omega_{\mathrm{c}}^2 + 2i\beta\omega_{\mathrm{c}} & \omega^2/(2n) \\ n\omega_{\mathrm{M}} & \omega - \omega_{\mathrm{m}} + i\alpha \end{pmatrix} \tag{6}$$

where $\omega_{\mathrm{c}} = 1/\sqrt{L_0 C}$ and $\beta = r_{\mathrm{circuit}}\sqrt{C/L_0}/2$ are the resonance angular frequency and the intrinsic damping of the (bare) RLC-circuit, respectively. Also, $\omega_{\mathrm{m}} = \omega_{\mathrm{H}} - \omega_{\mathrm{M}} + \omega_{\mathrm{K}}$ is the Kittel (magnon) mode, where $\omega_{\mathrm{H}} = \gamma\mu_0 H_0$, $\omega_{\mathrm{M}} = \gamma\mu_0 M_{\mathrm{s}}$, and $\omega = 2\gamma K_u/M_{\mathrm{s}}$. Hence, the hybridized eigenmodes are calculated by solving the determinant of Eq. (6):

$$\det\left(\bar{\Omega}(\omega)\right) = 0. \tag{7}$$

The influence of hybridization is usually most noticeable in a region near the crossing point, $\omega_{\mathrm{m}} = \omega_{\mathrm{c}}$, where the magnon and photon subsystems have similar resonance properties. Therefore, writing $\omega = \omega_{\mathrm{c}} + \delta$ with $\delta \ll \omega$, we can neglect terms of order δ^2 or δ/n. In addition, by implementing a classical version of the RWA, $\omega^2 - \omega_{\mathrm{c}}^2 \approx 2\omega_{\mathrm{c}}(\omega - \omega_{\mathrm{c}})$, we obtain the analytic dispersion for the hybridized modes

$$\omega_\pm = \left[(\tilde{\omega}_{\mathrm{c}} + \tilde{\omega}_{\mathrm{m}}) \pm \sqrt{(\tilde{\omega}_{\mathrm{c}} - \tilde{\omega}_{\mathrm{m}})^2 + \omega_{\mathrm{c}}\omega_{\mathrm{M}}}\right]/2, \tag{8}$$

where $\tilde{\omega}_{\mathrm{c}} = \omega_{\mathrm{c}} - i\beta\omega_{\mathrm{c}}$ and $\tilde{\omega}_{\mathrm{m}} = \omega_{\mathrm{m}} - i\alpha\omega_{\mathrm{c}}$. Therefore, we can write the effective non-Hermitian Hamiltonian of the coupled magnon-photon oscillator as

$$\hat{H} = \hbar\tilde{\omega}_{\mathrm{c}}\hat{a}^\dagger\hat{a} + \hbar\tilde{\omega}_{\mathrm{m}}\hat{m}^\dagger\hat{m} + \hbar\tilde{g}\left(\hat{a}^\dagger\hat{m} + \hat{m}^\dagger\hat{a}\right), \tag{9}$$

where $\hbar$ is the reduced Plank constant, $\hat{a}^\dagger$ ($\hat{a}$) and $\hat{m}^\dagger$ ($\hat{m}$) are the creation (annihilation) operators for photons and magnons, respectively, and

$$\tilde{g} \equiv (\omega_+ - \omega_-)/2 = \sqrt{-\omega_{\mathrm{c}}^2(\beta - \alpha)^2 + \omega_{\mathrm{c}}\omega_{\mathrm{M}}}/2. \tag{10}$$

Note that $2g = \mathrm{Re}[\omega_+] - \mathrm{Re}[\omega_-] \approx \sqrt{\omega_{\mathrm{c}}\omega_{\mathrm{M}}}/2$ is the Rabi-like splitting at the modes crossing point.

2.2 Scattering parameter

Using the coupled oscillator model in the previous section, we formulate the electric impedance of MP in an RLC-circuit with the dynamical inductor. We further calculate S_{21} being a scattering parameter for the microwave transmission measurement passing through the RLC-circuit.

A microwave network can be expressed in terms of scattering parameters, namely, the so-called S-parameters. The commonly used S-parameter for ferromagnetic resonance is S_{21} that can be interpreted as the power ratio of an incident wave (a_1) at port 1 and outgoing one (b_2) at port 2. For a two-port network with an input signal only in the port 1, it follows that $S_{21} = b_2/a_1$. Based on the standard microwave circuit theory,[26] we calculate S_{21} in our setup shown in Fig. 1 (a). Then, it is necessary to know the total impedance of the microwave circuit responsible for the resonance field inside the coil, which has contributions due to the current related with Ampère's law and the current induced via Faraday's law. The impedance of the RLC-circuit with current and field due to Ampère's law is given by Eq. (6),

$$Z_{\mathrm{A}}(\omega) = -i\frac{L_0}{\omega}\left(\omega^2 - \omega_{\mathrm{c}}^2 + 2i\beta\omega_{\mathrm{c}}\omega\right). \tag{11}$$

According to Eq. (4), an induced voltage due to the Faraday's low is $V_{\mathrm{F}} = -i\omega L_0 M_{\mathrm{s}} m_\perp/(2n)$. Then, for $m_\perp = -\gamma n I_0/(\omega - \omega_{\mathrm{m}} + i\alpha\omega)$, its impedance is calculated as

$$Z_{\mathrm{F}}(\omega) = i\frac{\omega L_0}{2}\frac{\omega_{\mathrm{M}}}{\omega - \omega_{\mathrm{m}} + i\alpha\omega}. \tag{12}$$

Now, we can calculate S_{21} based on the transmission ($ABCD$ or F) matrix approach. As shown in Fig. 1 (c), by coupling to the input and output through a cascade of the relevant matrix elements and treating the RLC-circuit as a shunt admittance, the transmission ($ABCD$ or F) matrix can be calculated as

$$\bar{F}(\omega) = \begin{pmatrix} A & B \\ C & D \end{pmatrix} = \bar{F}_M \bar{F}_{RLC}(\omega) \bar{F}_M^{-1} \tag{13}$$

with

$$\bar{F}_M = \begin{pmatrix} N_1/N_2 & 0 \\ 0 & N_2/N_1 \end{pmatrix}, \tag{14}$$

$$\bar{F}_{RLC}(\omega) = \begin{pmatrix} 1 & 0 \\ 1/Z_t(\omega) & 1 \end{pmatrix}, \tag{15}$$

where $Z_t(\omega) = Z_A(\omega) + Z_F(\omega)$ is the total impedance of the RLC-circuit and N_1/N_2 indicates the inductive coupling between the port and the RLC-circuit. Next, we relate the transmission matrix to the S-parameter. To this end, as shown in Fig. 1 (c), we assume microwave power vectors for incident, reflection, and transmission waves as (V_i, I_i), (V_r, I_r), and (V_t, I_t), respectively, which satisfy the following conditions:

$$\begin{pmatrix} V_i + V_r \\ I_i - I_r \end{pmatrix} = \bar{F}(\omega) \begin{pmatrix} V_t \\ I_t \end{pmatrix} \tag{16}$$

with $V_i/I_i = V_r/I_r = V_t/I_t = Z_0$. Here, Z_0 is the impedance of the microwave feedline. Regarding $S_{21} = V_t/V_i$ in our two-port network and solving Eq. (16), the S-parameter for the microwave transmission measurement is therefore

$$S_{21} = \frac{2Z_0}{AZ_0 + B + CZ_0^2 + DZ_0} = \frac{Z_t(\omega)}{Z_t(\omega) + 4\beta_{ex}\omega_c L_0}, \tag{17}$$

where $\beta_{ex} = N_2^2 Z_0/(8N_1^2\omega_c L_0)$ is the extrinsic damping parameter of the RLC-circuit.

3. Results and Discussion

Towards the experimental demonstration of the room temperature ultrastrong-coupled MP, we use realistic parameters for MI, which are those of yttrium iron garnet (YIG)[23,27] with $\gamma = 1.76 \times 10^{11}$ T^{-1}s^{-1}, $\alpha \approx 10^{-4}$, and $M_s \approx 120$ kAm^{-1}. We also disregard the very low in-plane magnetocrystalline anisotropy field~ 0.3 mT reported.[28] Note that YIG is typically used in magnonics as a high-performance material.[29-31] For dimensions etc. of the coil, we assume $l = w = 1.0$ mm and $n = 100$ mm^{-1}, which gives $L_0 \approx 1.3$ nH for $d_M = 100$ nm. Also, $C = 1.0$ pF is used within realistic values.

Figure 2 shows calculated eigen-frequency ($\mathrm{Re}[\omega_\pm]$) of the MP hybridized mode with/without RWA for different values of d_M. The results for with/without RWA are calculated by Eqs. (8) and (7), respectively. Also, these calculated results are also highlighted in Tables I and II. In the case for $d_M = 10$ nm, one can see a huge level repulsion characterized by the Rabi-like splitting $2g/(2\pi) \approx 7.9$ GHz for w/o RAW and 7.7 GHz for w/ RWA, whose values are more than a half of the circuit mode $\omega_c/(2\pi) \approx 14.2$ GHz. Then, the coupling ratio is $g/\omega_c \approx 0.28$ (0.27) without (with) RWA, which means that the MP based on the dynamical inductor is in the USC regime. Accordingly, the MP has the cooperativity $C_{RLC} = g^2/(\alpha\beta\omega_c^2) \approx 1.7 \times 10^4$ for both cases with $\beta = 4.5 \times 10^{-2}$. In the USC regime, the breakdown of the RWA makes the system possess eigenstates combined by various states with different particle numbers, which modifies the Rabi spiting via the Bloch-Siegert shift mechanism. However, the RWA in the current system still keeps the meaning because of a relatively small coupling ratio ($g/\omega_c \lesssim 0.28$) even for the USC regime, which is supported by the Dicke model.[18),32] In the case for $d_M = 100$nm, the magnitude of $2g/(2\pi)$ is around 4.9 GHz for w/o RAW and 4.4 GHz for w/ RWA, whose values are comparable to that of the circuit mode $\omega_c/(2\pi) \approx 4.5$ GHz. Then, the coupling ratio is $g/\omega_c \approx 0.55$ (0.49) without (with) RWA, which indicates that the dynamical inductor-based MP approaches to the deep-strong coupling regime (defined for $g/\omega_c \gtrsim 1$).[18] Also, the corresponding cooperativity $C_{RLC} \approx 2.1$ (1.7) $\times 10^5$ is enhanced for each case with $\beta = 1.4 \times 10^{-2}$. In contrast to the result for $d_M = 10$ nm, the RWA appears to break down, resulting in a larger shift of the Rabi-like spiting.

Table 1 Calculated results for $d_M = 10$ nm.

Indexes	w/o RWA	w/ RWA
$2g/(2\pi)$ [GHz]	7.9	7.7
$\omega_c/(2\pi)$ [GHz]	14.2	142.
g/ω_c	0.28	0.27
$C_{RLC} = g^2/(\alpha\beta\omega_c^2)$	1.7×10^4	1.7×10^4

Table 2 Calculated results for $d_M = 100$ nm.

Indexes	w/o RWA	w/ RWA
$2g/(2\pi)$ [GHz]	4.9	4.4
$\omega_c/(2\pi)$ [GHz]	4.5	4.5
g/ω_c	0.55	0.49
$C_{RLC} = g^2/(\alpha\beta\omega_c^2)$	2.1×10^5	1.7×10^5

Figure 3 shows the computed scattering parameter ($|S_{21}|^2$) of the MP hybridized mode without RWA based on Eq. (17) for different values of d_M. The impedance of the microwave feedline $Z_0 = 50$ Ω is assumed to be larger than the circuit one ($r_{circuit} = 1.0$ Ω). Also, we set the inductive coupling $N_1/N_2 = 0.3$. These parameters lead to $\beta = 4.5(1.4) \times 10^{-2}$ and $\beta_{ex} = 5.0(1.6) \times 10^{-2}$ for given L_0 with $d_M = 10(100)$ nm and $C = 1.0$ pF. As seen in these figures, an input microwave power is absorbed by the MP, i.e., $|S_{21}|^2$ rapidly decreases at the eigen-frequency ($\mathrm{Re}[\omega_\pm]$) displayed on Fig. 2. Since the level broadening in S_{21} depends on the magnitude of the intrinsic damping (β), $|S_{21}|^2$ for $d_M = 100$ nm has a narrower linewidth than that for $d_M = 10$ nm. Therefore, by tunning the size (d_M) of the dynamical inductor, the experiment might realize an ideal ultrastrong-coupled MP which possesses a larger coupling ratio (g/ω_c) and higher cooperativity (C_{RLC}) at room temperature. In actuality, a similar MP near the USC regime is observed in a metamolecule consisting of a coil involving a ferrite (YIG) rod.[33] For such a measurement, the capability of the magnetic damping constant (α) could be up to an order of 10^{-2}, whose value is comparable to that of the circuit mode (β). For circuit parameters used here, input microwave power is an order of mW which needs to excite

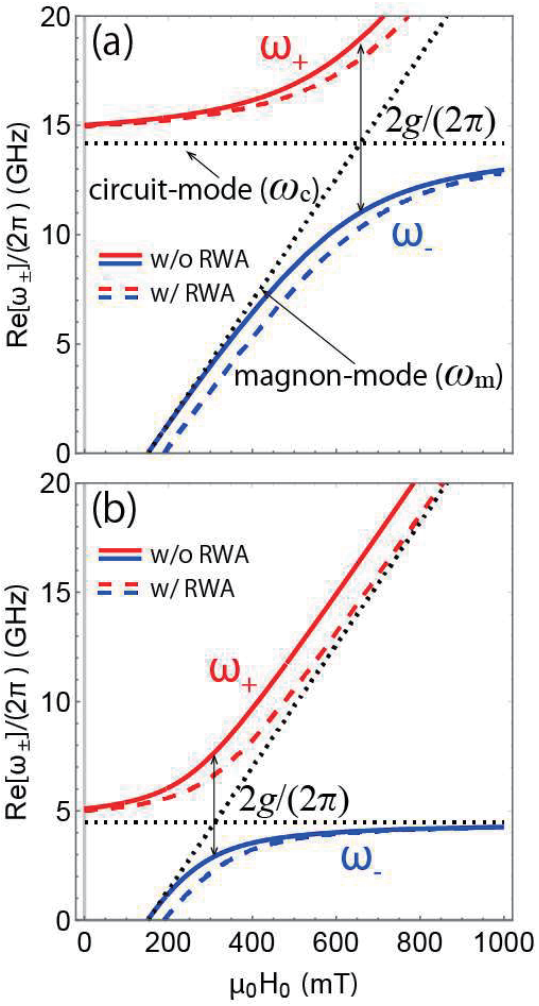

Fig. 2 Calculated eigen-frequency (Re[$\omega_\pm$]) of the MP hybridized mode as a function of an external magnetic field ($\mu_0 H_0$) for (a) $d_M = 10$ nm and (b) $d_M = 100$ nm. In these plots, $r_{circuit} = 1.0\ \Omega$ is used.

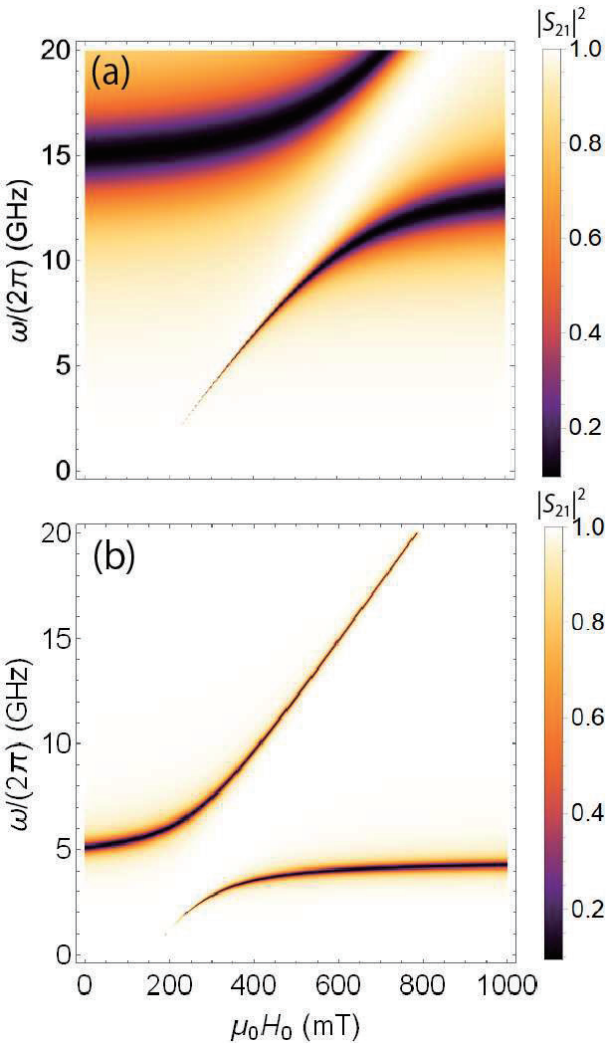

Fig. 3 Computed $|S_{21}|^2$ as functions of an external magnetic field ($\mu_0 H_0$) and a microwave frequency ($\omega/(2\pi)$) for (a) $d_M = 10$ nm and (b) $d_M = 100$ nm. The details of the calculations are given in the text.

the ferromagnetic resonance of MI and the estimated inductance is an order of nH, so that for a resonance frequency even with 14.2 GHz (for MI with 10 nm) the corresponding impedance is several tens Ω, whose value is comparable to that of the microwave feedline (50 Ω is assumed). Hence, the reflection of the input microwave would not suffer from the so-called impedance mismatch problem.

In addition, we mention a guideline to achieve the deep-strong coupled MP in the dynamical inductor. To this end, we show computed coupling ratio (g/ω_c) as a function of $\omega_c/(2\pi)$ in Fig. 4. As we have discussed above, the magnitude of the Rabi-like splitting ($\propto g$) increases with decreasing the size of the coil (d_M). In contrast, the coupling ratio shows the opposite trend, i.e., g/ω_c is roughly proportional to $d_M^{1/4}$ via L_0 in the circuit mode ω_c. Accordingly, a plausible strategy for deep-strong coupling is to enhance the coupling ratio by a reduced resonance frequency, which could be easily conducted by tuning the coil size. As shown in Fig. 4, the estimated coil size is around $d_M = 1$ μm to reach the deep-strong coupling regime in the dynamical inductor. This strategy is sharp contrast to that of cavity/planar-resonator based magnonics which attempt to enhance the coupling ratio by scaling down the mode volume.[16,17]

Finally, we briefly mention potential applications of the proposed ultrastrong coupled MP toward the quantum information technology. The candidate one is quantum handling of the single magnon excitation using the box cavity demonstrated by *Tabuchi et al.* in Ref. 5. For the magnetic flux type qubits, an added coil to the *RLC*-circuit in Fig. 1 (a) might be used for a magnon-qubit coupling. Then, USC of the proposed MP could allow us to conduct a much faster measurement and control for the single magnon excitation. Note that we need to replace circuit components (leads etc.) by superconducting ones. Other candidate is MP based

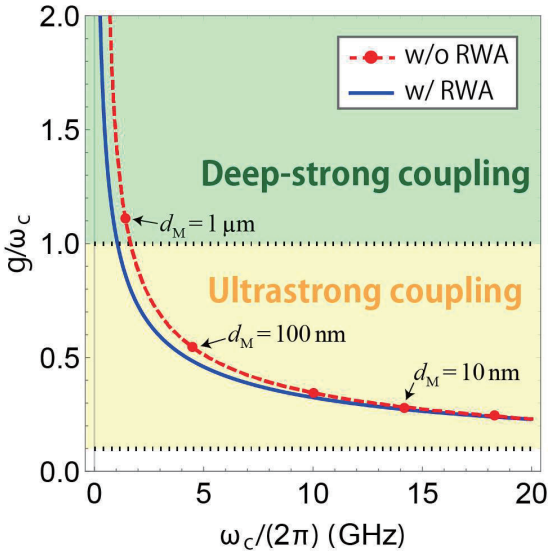

Fig. 4 Computed coupling ratio (g/ω_c) of the MP hybridized mode as a function of $\omega_c/(2\pi)$. The dashed red line is a fitting function for the w/o RWA case by $f(x) = a/\sqrt{b + cx + dx^2}$ with $x = \omega_c/(2\pi)$. In this plot, $r_{\mathrm{circuit}} = 1.0\ \Omega$ is used.

masers,[7] coherent microwave emitters, for control of quantum information devices. Instead of the box cavity used in Ref. 7, the proposed dynamical inductor with the ultrastrong coupled MP might be useful to stabilize the coherent microwave emission.

4. Summary

In summary, we have presented a microwave transmission theory for an ultrastrong-coupled MP in dynamical inductors which consist of a coil involving a magnetic insulator. Combining with the *RLC*-circuit and LLG equations, we formulated the electric impedance of MP as a coupled oscillator under the corresponding principle. Based on the transmission (*ABCD* or *F*) matrix approach, we further calculate a scattering parameter for the microwave transmission measurement (S_{21}) passing through an *RLC*-circuit with the dynamical inductor. By tunning the size ($d \approx d_{\mathrm{M}}$) of the coil, we theoretically demonstrated an on-chip ultrastrong-coupled MP at room temperature, which reaches a coupling ratio $g/\omega_c \approx 0.55$ and cooperativity $C_{RLC} \approx 2 \times 10^5$ with material parameters of YIG. In addition, we showed a strategy to achieve the deep-strong coupled MP in the dynamical inductor.

Acknowledgments The authors thank Satoshi Tomita, Toshiyuki Kodama, Jun-ichiro Ohe, Hiroaki Matsueda, and Ryunosuke Suzuki for valuable discussions. This work was supported by Grants-in-Aid for Scientific research (Grants No. 22K14591, No. 20H02196, and No. 20K03814) from the Japan Society for the Promotion of Science.

References

1) M. Harder, B. M. Yao, Y. S. Gui, and C. -M. Hu: *J. Appl. Phys.*, **129**, 201101 (2021).
2) D. L.-Quirion, S. P. Wolski, Y. Tabuchi, S. Kono, K. Usami, and Y. Nakamura: *Science*, **367**, 425 (2020).
3) X. Zhang, C. -L. Zou, N. Zhu, F. Marquardt, L. Jiang, and H. X. Tang: *Nat. Commun.*, **6**, 8914 (2015).
4) R. -C. Shen, Y. -P.Wang, J. Li, S. -Y. Zhu, G. S. Agarwal, and J. Q. You: *Phys. Rev. Lett.*, **127**, 183202 (2021).
5) Y. Tabuchi, S. Ishino, A. Noguchi, T. Ishikawa, R. Yamazaki, K. Usami, and Y. Nakamura: *Science*, **349**, 405 (2015).
6) J. A. Haigh, A. Nunnenkamp, A. J. Ramsay, and A. J. Ferguson: *Phys. Rev. Lett.*, **117**, 133602 (2016).
7) B. Yao, Y. S. Gui, J.W. Rao, Y. H. Zhang,Wei Lu, and C. -M. Hu: *Phys. Rev. Lett.*, **130**, 146702 (2023).
8) Y. Li, T. Polakovic, Y. -L.Wang, J. Xu, S. Lendinez, Z. Zhang, J. Ding, T. Khaire, H. Saglam, R. Divan, J. Pearson, W. -K. Kwok, Z. Xiao, V. Novosad, A. Hoffmann, and W. Zhang: *Phys. Rev. Lett.*, **123**, 107701 (2019).
9) J. T. Hou and L. Liu: Phys. Rev. Lett., **123**, 107702 (2019).
10) V. Castel, R. Jeunehomme, J. B. Youssef, N. Vukadinovic, A. Manchec, F. K. Dejene, and G. E. W. Bauer: *Phys. Rev. B*, **96**, 064407 (2017).
11) Y. Yang, J. W. Rao, Y.S. Gui, B. M. Yao, W. Lu, and C. -M. Hu: *Phys. Rev. Applied*, **11**, 054023 (2019).
12) D. L.-Quirion, Y. Tabuchi, A. Gloppe, K. Usami, and Y. Nakamura: *Appl. Phys. Express*, **12**, 070101 (2019).
13) A. Barman, G. Gubbiotti, S. Ladak, A. O. Adeyeye, M. Krawczyk, J. Gr¨afe, C. Adelmann, S. Cotofana, A. Naeemi, V. I. Vasyuchka et al.: *J. Phys.: Condens. Matter*, **33**, 413001 (2021).
14) H. Y. Yuan, Y. Cao, A. Kamra, R. A. Duine, P. Yan: *Phys. Rep.*, **965**, 26 (2022).
15) B. Z. Rameshti, S. V. Kusminskiy, J. A. Haigh, K. Usami, D. L. -Quirion, Y. Nakamura, C. -M. Hu, H. X. Tang, G. E. Bauer, and Y. M. Blanter: *Phys. Rep.*, **979**, 1 (2022).
16) I. A. Golovchanskiy, N. N. Abramov, V. S. Stolyarov, M. Weides, V. V. Ryazanov, A. A. Golubov, A. V. Ustinov, and M. Y. Kupriyanov: *Sci. Adv.*, **7**, eabe8638 (2021).
17) I. A. Golovchanskiy, N. N. Abramov, V. S. Stolyarov, A. A. Golubov, M. Y. Kupriyanov, V. V. Ryazanov, and A. V. Ustinov: *Phys. Rev. Applied*, **16**, 034029 (2021).
18) A. F. Kockum, A. Miranowicz, S. D. Liberato, S. Savasta, and F. Nori: *Nat. Rev. Phys.*, **1**, 19 (2019).
19) T. Chiba, T. Komine, and T. Aono: *Appl. Phys. Lett.*, in press.
20) T. Chiba and T. Komine: *Phys. Rev. Applied*, **14**, 034031 (2020).
21) T. Chiba, A. O. Leon, and T. Komine: *Appl. Phys. Lett.*, **118**, 252402 (2021).
22) T. Liu, J. Kally, T. Pillsbury, C. Liu, H. Chang, J. Ding, Y. Cheng, M. Hilse, R. E. -Herbert, A. Richardella, N. Samarth, and M. Wu: *Phys. Rev. Lett.*, **125**, 017204 (2020).
23) J. Ding, C. Liu, Y. Zhang, U. Erugu, Z. Quan, R. Yu, E. McCollum, S. Mo, S. Yang, H. Ding, X. Xu, J. Tang, X. Yang, and M. Wu: *Phys. Rev. Applied*, **14**, 014017 (2020).
24) L. Soumah, N. Beaulieu, L. Qassym, C. Carrétéro, E. Jacquet, R. Lebourgeois, J. Ben Youssef, P. Bortolotti, V. Cros, and A. Anane: *Nat. Commun.*, **9**, 3355 (2018).
25) C. Tang, L. Alahmed, M. Mahdi, Y. Xiong, J. Inman, N. J. McLaughlin, C. Zollitsch, T. H. Kim, C. R. Du, H. Kurebayashi et al.: *arXiv*:2301.09822.
26) D. M. Pozar, *Microwave Engineering*, 4th ed. (John Wiley & Sons, Inc., 2011).
27) M. Schreier, T. Chiba, A. Niedermayr, J.Lotze, H. Huebl, S. Geprägs, S. Takahashi, G. E. W. Bauer, R. Gross, and S. T. B. Goennenwein: *Phys. Rev. B*, **92**, 144411 (2015).
28) N. Vlietstra, J. Shan, V. Castel, B. J. van Wees, and J. Ben Youssef: *Phys. Rev. B*, **87**, 184421 (2013).

29) Y. Kajiwara, K. Harii, S. Takahashi, J. Ohe, K. Uchida, M. Mizuguchi, H. Umezawa, H. Kawai, K. Ando, K. Takanashi, S. Maekawa, and E. Saitoh: *Nature,* **464**, 262 (2010).
30) T. Chiba, G. E. W. Bauer, and S. Takahashi: *Phys. Rev. Applied,* **2**, 034003 (2014).
31) L. Bai, M. Harder, Y. P. Chen, X. Fan, J. Q. Xiao, and C. -M. Hu: *Phys. Rev. Lett.*, **114**, 227201 (2015).
32) P. Kirton, M. M. Roses, J. Keeling, and E. G. D. Torre: *Adv. Quantum Technol.*, **2**, 1800043 (2019).
33) S. Tomita, H. Kurosawa, K. Sawada, and T. Ueda: *Phys. Rev. B*, **95**, 085402 (2017).

Received Oct. 13, 2023; Accepted Dec. 13, 2023

J. Magn. Soc. Jpn., **48**, 28-33 (2024) <Paper>

Evaluation of Spin Hall Effect in Ferromagnets by Means of Unidirectional Spin Hall Magnetoresistance in Ta/Co Bilayers

M. Aoki[a),b)†], R. Ohshima[a),b)], T. Shinjo[a)], M. Shiraishi[a),b)], and Y. Ando[a),b),c)]
a) Department of Electric Science and Engineering, Kyoto Univ., *Kyoto Univ. Katsura, Nishikyo-ku, Kyoto, Kyoto 615-8510, Japan*
b) Center for Spintronics Research Network, Institute of Chemical Research, Kyoto Univ., *Gokasho, Uji, Kyoto 611-0011, Japan*
c) PRESTO, Japan Science and Technology Agency, *4-1-8 Honcho, Kawaguchi, Saitama 332-0012, Japan*

We investigate unidirectional spin Hall magnetoresistance (USMR) in Ta/Co bilayer systems with various Co thicknesses. A negative USMR is observed when the thickness of Co is thin due to the negative spin Hall angle of Ta, as expected from the conventional framework. However, as the Co thickness increases, the amplitude of USMR becomes strongly suppressed, and the sign of USMR becomes positive, which cannot be explained by theoretical calculation considering only the spin Hall effect (SHE) in the Ta layer. We successfully explain the anomalous thickness dependence of USMR by considering USMR induced by SHE in the Co layer. This work verifies the significant influence of SHE in ferromagnets on the measurement of USMR and will contribute to a better understanding of USMR.

Keywords: spintronics, spin Hall effect, unidirectional spin Hall magnetoresistance, spin current

1. Introduction

Magnetoresistance (MR) effects have been intensively investigated since the 19th century, and a variety of MR effects have been observed in ferromagnetic materials (FM)[1], topological insulators[2,3], Weyl semimetals[4], and two-dimensional materials[5]. In most cases, the sign and magnitude of MR do not change under sign reversal of a magnetic field/magnetization, i.e., an even function of a magnetic field/magnetization. Therefore, whereas most MR effects are applicable to the detection of magnetic field/magnetization rotation by 90 degrees, they cannot be used for the detection of such rotation by 180 degrees, i.e., magnetization/magnetic field reversal. Since the detection of magnetization reversal by MR can be applied to the reading process of magnetoresistive random access memory without the need to fabricate additional electrodes[6], MR, which has an odd function of magnetization, is attracting much attention. A representative example of such odd-function MR effects is unidirectional spin Hall magnetoresistance (USMR) [7–12] in a nonmagnetic material (NM)/FM bilayer system.

Figures 1(a) and 1(c) show schematics of the mechanism of USMR when the electric current in the NM layer, $J_{c(N)}$, is positive and negative, respectively. $J_{c(N)}$ is converted to spin current, $J_{s(N)}$, via the spin Hall effect (SHE)[13]. Then, injection of spin into FM causes fluctuation in the population of spins parallel or anti-parallel to the magnetization, $\boldsymbol{M}$, in the FM layer. Since parallel and anti-parallel spins do not degenerate in FM and have different electron mobilities with each other, fluctuation of parallel- or anti-parallel-spin populations results in fluctuation in the resistivity in the FM[10]. Injected spin polarization, i.e., parallel or anti-parallel spins, is reversed when the direction of $J_{c(N)}$ or magnetization of the FM is reversed, meaning that the resistance of the NM/FM bilayer changes depending on the direction of $J_{c(N)}$ and magnetization.

Aiming at application for the detection of magnetization reversal, researchers have focused on NMs with a large spin Hall angle (SHA), which is an indicator of the magnitude of SHE, such as heavy metals and topological insulators[14], because they enable larger spin-current injection and larger USMR. However, SHE in the FM layer has been overlooked. Recent findings on sizable SHE in FM[15–19] indicate that USMR would also be induced by SHE in the FM layer [self-induced USMR, (SI-USMR)] as explained as follows.

Figures 1(b) and 1(d) show schematics of the mechanism of SI-USMR when the electric current in the FM layer, $J_{c(F)}$, is positive and negative, respectively. $J_{c(F)}$ is converted to spin current, $J_{s(F)}$, via the SHE in the FM layer. Then, extraction of spin from FM causes

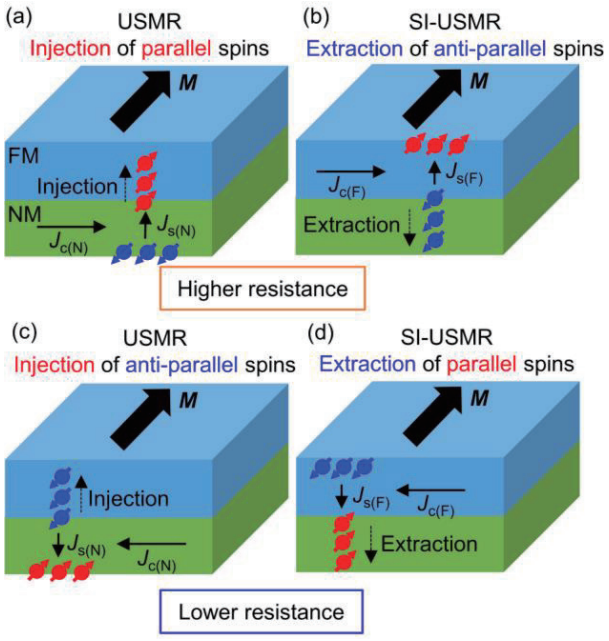

Fig. 1 Schematics of the mechanism of (a) USMR when $J_{c(N)}$ is positive, (b) SI-USMR when $J_{c(F)}$ is positive, (c) USMR when $J_{c(N)}$ is negative, and (d) SI-USMR when $J_{c(F)}$ is negative. In these schematics, SHAs of NM and FM are positive.

Corresponding author:
M. Aoki (e-mail: aoki.motomi.53r@st.kyoto-u.ac.jp).

fluctuation in the population of spins parallel or anti-parallel to $\boldsymbol{M}$ in the FM layer, resulting in a change in resistivity in the same manner as USMR originating from SHE in the NM layer. Since injection of parallel (anti-parallel) spins into the FM and extraction of anti-parallel (parallel) spins from the FM are attributed to the positive (negative) SHA in the NM and FM with a positive electric current, respectively, relationships between signs of the SHA and fluctuation of the resistivity are the same in USMR and SI-USMR. Although SI-USMR is predicted to exist theoretically[12], it has not been experimentally unveiled yet if it is present in NM/FM systems.

In this research, we estimated the influence of SI-USMR in Ta/Co bilayer systems, where sizable self-induced spin-orbit torque (SI-SOT) due to SHE in the Co layer was confirmed in our previous work[20]. We compared the thickness dependence of experimentally observed USMR signals with theoretical models that do and do not consider SHE in the FM layer. As a result, a theoretical model considering SHE in the Co layer well explains experimental results, indicating the existence of SI-USMR due to SHE in the Co layer. From analysis using a model equation, we estimate the SHA of Ta and Co to be −0.2 and 0.05, respectively. Our result shows the significant influence of SHE in FM on USMR in NM/FM systems and will contribute to a better understanding of USMR in NM/FM bilayer systems.

2. Device fabrication and experimental procedure

Figure 2(a) shows schematics of the device structure and electrical circuits used in this study. Hall bars made of Ta(5)/Co(t_F)/SiO_2(7) layers were fabricated using electron-beam (EB) lithography and DC magnetron sputtering. Then, electrode structures were drawn by EB lithography, and a SiO_2 layer was etched by Ar^+ ion milling to make an Ohmic contact. Samples were transported to an EB deposition system without breaking the vacuum, and a Ti(3)/Au(70) electrode was deposited. Here, numbers in brackets are the thickness in nanometers. We measured longitudinal and transverse second harmonic voltages, $V_{xx}^{2\omega}$ and $V_{xy}^{2\omega}$, using a lock-in amplifier (Stanford SR 830) and AC-DC current source (Keithley 6221).

Here, we explain the advantage of using lock-in technique for the experiment of USMR. In principle, USMR can be detected even by using a DC current and a DC voltmeter. However, large offset coming from the longitudinal resistance makes it difficult to estimate USMR. In contrast, harmonic measurement by applying an AC current with a frequency of ω enables us to remove such a large offset because voltage induced by USMR is proportional to the square of the current and oscillate with 2ω, whereas voltage from the longitudinal resistance is linear to the current and oscillate with ω.

Longitudinal (transverse) second harmonic resistance, $R_{xx}^{2\omega}$ ($R_{xy}^{2\omega}$), was calculated by $R_{xx}^{2\omega}(R_{xy}^{2\omega}) = V_{xx}^{2\omega}(V_{xy}^{2\omega})/\sqrt{2}\,I_{ac}$, where I_{ac} is the amplitude of the AC current, which was fixed at 10 mA for devices with t_F = 4 nm and 5 nm, whereas it was fixed at 20 mA for devices with $t_F \geqq 7$ nm to increase the current density. The frequency of I_{ac} was fixed at 17 Hz. A magnetic field, H_{ext}, was applied in-plane in a physical property measurement system (Quantum Design PPMS), where the angle between H_{ext} and x axis was defined as φ. All measurements were carried out at room temperature.

3. Observation of unidirectional spin Hall magnetoresistance by second harmonic measurements

3.1 Longitudinal measurements

Figure 2(b) shows $R_{xx}^{2\omega}$ as a function of φ with $\mu_0 H_{ext}$ = 4 T for the Ta(5)/Co(5) device. A black line indicates fitting using[10),21)],

$$R_{xx}^{2\omega} = \left(R_{USMR} + R_{ANE(L)} + \alpha_{ONE(L)} H_{ext}\right)\sin\varphi + R_{FLT(L)}\sin\varphi\cos^2\varphi + R_{PNE(L)}\cos 2(\varphi - \varphi_0), \quad (1)$$

where R_{USMR}, $R_{ANE(L)}$, $\alpha_{ONE(L)}H_{ext}$, $R_{FL\,SOT}$, and $R_{PNE(L)}$ are longitudinal second harmonic resistance generated by USMR, the anomalous Nernst effect (ANE), the ordinary Nernst effect (ONE), field-like torque (FLT), which includes both the field-like SOT and torque due to the

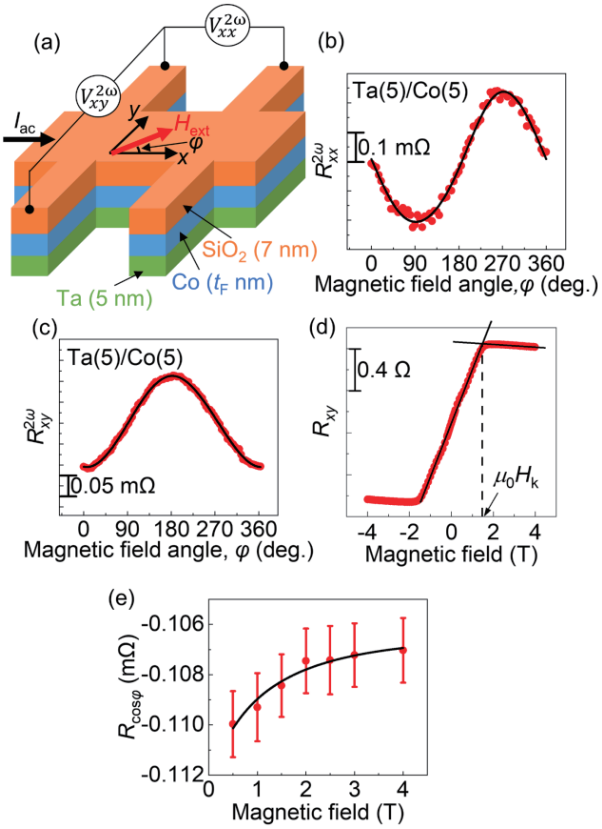

Fig. 2 (a) Schematics of device structure and measurement circuit used in this study. (b) Longitudinal and (c) transverse second harmonic resistance as function of φ measured for Ta(5)/Co(5) bilayer system with $\mu_0 H_{ext}$ = 4 T. (d) Transverse resistance as function of $\mu_0 H_{ext}$ applied out-of-plane. DC electric current with amplitude of 1 mA was applied in this measurement. Black lines indicate linear fittings, where magnetization was and was not saturated. Magnetic field at intercept of two fitting lines corresponds to $\mu_0 H_k$. (e) $R_{\cos\varphi}$ as function of $\mu_0 H_{ext}$ measured for Ta(5)/Co(5) system. Red dots are measured signal, and black curves indicate fitted result.

Oersted field, and the planar Nernst effect (PNE), respectively. Offset angle, φ_0, is considered in the PNE contribution because direction of in-plane thermal gradient is not well-defined. Although FLT and PNE are eliminated by measuring $R_{xx}^{2\omega}$ as a function of φ, ANE and ONE cannot be eliminated because they have the same φ dependence as that of USMR.

3.2 Transverse measurements

To extract R_{USMR} from $R_{xx}^{2\omega}$, we measured $R_{xy}^{2\omega}$ as a function of φ. Figure 2(c) shows $R_{xy}^{2\omega}$ as a function of φ with $\mu_0 H_{\mathrm{ext}}$ = 4 T for the Ta(5)/Co(5) device. A black line indicates fitting using[21]:

$$R_{xy}^{2\omega} = R_{\cos\varphi}\cos\varphi + R_{\mathrm{FLT(T)}}(2\cos^3\varphi - \cos\varphi) + R_{\mathrm{PNE(T)}}\sin 2(\varphi - \varphi_0), \quad (2)$$

where $R_{\mathrm{FLT(T)}}$ and $R_{\mathrm{PNE(T)}}$ are transverse second harmonic resistance generated by FLT and PNE. $R_{\cos\varphi}$ is expressed as[22]:

$$R_{\cos\varphi} = \frac{\alpha_{\mathrm{DL}}}{H_{\mathrm{ext}} + H_{\mathrm{k}}} + R_{\mathrm{ANE(T)}} + \alpha_{\mathrm{ONE(T)}} H_{\mathrm{ext}}, \quad (3)$$

where H_{k} is the in-plane anisotropy field. $\alpha_{\mathrm{DL}}/(H_{\mathrm{ext}} + H_{\mathrm{k}})$, $R_{\mathrm{ANE(T)}}$, and $\alpha_{\mathrm{ONE(T)}} H_{\mathrm{ext}}$ are transverse second harmonic resistance generated by damping-like SOT (DL SOT), ANE, and ONE, respectively. Here, H_{k} was independently estimated from the measurement of the anomalous Hall effect as shown in Fig. 2(d). Although DL SOT, ANE, and ONE have the same φ dependence, they have different dependences on H_{ext}, meaning that $R_{\mathrm{ANE(T)}}$ and $\alpha_{\mathrm{ONE(T)}}$ can be estimated from the H_{ext} dependence of $R_{\cos\varphi}$ as shown in Fig. 2(e).

3.3 Contribution of anomalous Nernst effect

From the measurements in Section 3.1 and 3.2, $R_{\mathrm{USMR}} + R_{\mathrm{ANE(L)}} + \alpha_{\mathrm{ONE(L)}} H_{\mathrm{ext}}$, $R_{\mathrm{ANE(T)}}$, and $\alpha_{\mathrm{ONE(T)}} H_{\mathrm{ext}}$ are estimated. To estimate R_{USMR}, $R_{\mathrm{ANE(L)}}$ and $\alpha_{\mathrm{ONE(L)}} H_{\mathrm{ext}}$ need to be converted from $R_{\mathrm{ANE(T)}}$ and $\alpha_{\mathrm{ONE(T)}} H_{\mathrm{ext}}$, respectively. Figures 3(a) and 3(b) show the relationship between thermoelectric voltages generated along transverse and longitudinal directions, respectively. An electric field due to ANE and ONE, $\boldsymbol{E}_{\mathrm{ANE+ONE}}$, is produced along the cross product of magnetization, $\boldsymbol{M}$, and temperature gradient, ∇T. We note that ANE and ONE has the same symmetry with φ in this experiment because amplitude of H_{ext} is large enough to align magnetization along H_{ext}. Since ∇T generated by Joule heating and the heat-sink effect of the MgO substrate is independent of the magnetization direction, the magnitude of $\boldsymbol{E}_{\mathrm{ANE+ONE}}$ is also independent of the magnetization direction. Therefore, longitudinal and transverse thermoelectric resistances are simply correlated by the geometry of the Hall bar[7]. When we define distances between the two electrodes used in longitudinal and transverse measurements as l and w, respectively, $R_{\mathrm{ANE(L)}} + \alpha_{\mathrm{ONE(L)}} H_{\mathrm{ext}}$ is simply calculated by:

$$R_{\mathrm{ANE(L)}} + \alpha_{\mathrm{ONE(L)}} H_{\mathrm{ext}} = \frac{l}{w}\left(R_{\mathrm{ANE(T)}} + \alpha_{\mathrm{ONE(T)}} H_{\mathrm{ext}}\right). \quad (4)$$

Figures 3(c) and 3(d) show the contributions from USMR and ANE + ONE in $R_{xx}^{2\omega}/I_{ac}$ for Ta(5)/Co(5) and Ta(5)/Co(17.5) devices, respectively. In both cases, signals were well fitted by Eq. (1), and the contribution from USMR was successfully separated from that from thermoelectric effects.

$R_{xx}^{2\omega}$ shows complicated φ dependence at t_{F} = 17.5 nm as shown in Fig. 3(d) because contributions from Oersted field ($\sin 2\varphi \sin\varphi$) and PNE ($\cos 2\varphi$) becomes salient as t_{F} increases. However, we emphasize that contribution from the USMR is properly estimated even at t_{F} = 17.5 nm because the measured plots are well fitted by Eq. (1).

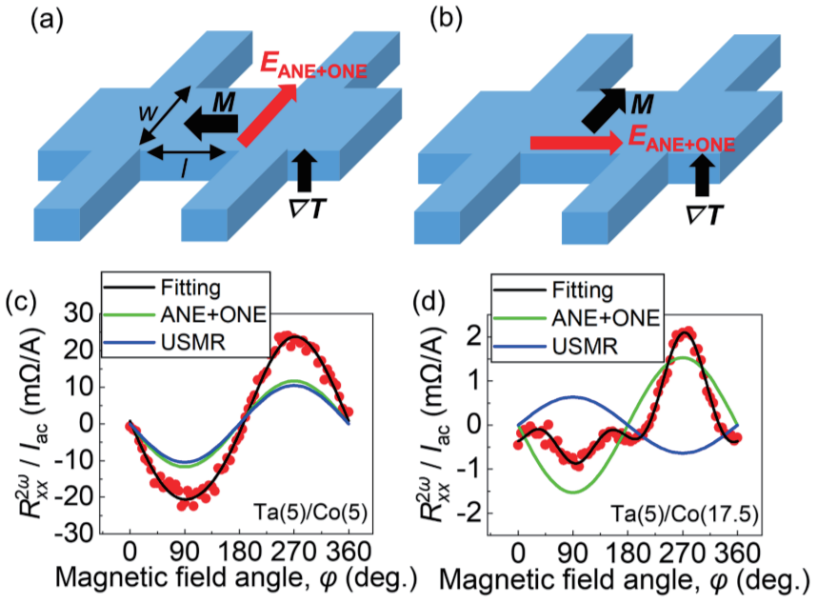

Fig. 3 (a) Schematics of generation of thermoelectric signals when $\boldsymbol{M}$ is along longitudinal direction of Hall bar and (b) transverse direction of Hall bar. In our experiment, l and w were 45 μm and 40 μm, respectively. (c) $R_{xx}^{2\omega}/I_{\mathrm{ac}}$ as a function of φ for Ta(5)/Co(5) and (d) Ta(5)/Co(17.5) devices. Contributions from thermoelectric signals and USMR are shown as green and blue curves, respectively.

4. Theoretical analysis of thickness dependence of unidirectional spin Hall magnetoresistance

4.1 Thickness dependence of unidirectional spin Hall magnetoresistance

We estimated the USMR for Ta/Co devices with different t_F following the procedure in Section 3. Figure 4(a) shows the USMR coefficient normalized by current amplitude, $\alpha_{USMR} / I_{ac} = R_{USMR} / (I_{ac} R)$, as a function of t_F, where R is the four-terminal resistance of the Ta/Co devices. α_{USMR} / I_{ac} showed a negative value when t_F was thin, which is consistent with the scenario that USMR is induced by SHE in Ta because $\alpha_{USMR} \sim \theta_N$, where θ_N is the SHA of the NM layer (−0.1 ~ −0.2 in Ta)[8),11)]. However, α_{USMR} / I_{ac} was strongly suppressed and became almost zero when t_F was thicker than ~ 14 nm, indicating that the contribution of SHE in Ta became suppressed as t_F got thicker. Given that the SHA of Co is positive[16)] and cancels the contribution from the negative SHE in Ta[23)], it is likely that SI-USMR originating from Co was enhanced and caused anomalous suppression of the net USMR as t_F became thicker.

One might think that positive USMR at t_F = 17.5 nm is attributed to imperfection in the conversion of thermoelectric signals. If the conversion coefficient from transverse to longitudinal thermoelectric signal is smaller than l / w because of misalignment in the fabrication process, sign of USMR could be negative even at t_F = 17.5 nm. However, to make α_{USMR} / I_{ac} positive at t_F = 17.5 nm, the conversion coefficient needs to be less than 60 % of the actual value of l/ w. Given that we use EB lithography in all the drawing processes of the Hall bar structure and the misalignment of the drawing is typically less than 100 nm, which is much less than 1 % of the value of l and/or w, we conclude that imperfection in device structure cannot explain sign reversal of the USMR at t_F = 17.5 nm.

4.2 Analysis without considering self-induced unidirectional spin Hall magnetoresistance

To support our assumption that the strong suppression of USMR when t_F is thick is due to SI-USMR originating from Co, we compared experimental results and theoretical calculations. Figure 4(b) shows the thickness evolution of α_{USMR} / I_{ac} calculated by[8),12)]:

$$\frac{\alpha_{USMR}}{I_{ac}} = \frac{e(p_\sigma - p_N)\tanh\left(\frac{t_F}{\lambda_F}\right)}{1 + (1 - p_\sigma^2)\left(\frac{\sigma_F \lambda_N}{\sigma_N \lambda_F}\right)\tanh\left(\frac{t_F}{\lambda_F}\right)\coth\left(\frac{t_N}{\lambda_N}\right)} \times \left[\left(\frac{\theta_N \lambda_N}{\varepsilon_F}\right)\tanh\left(\frac{t_N}{2\lambda_N}\right) + \left(\frac{\theta_F \lambda_F}{\varepsilon_F}\right)\tanh\left(\frac{t_F}{2\lambda_F}\right)\right] \times \frac{3R}{2l}, \quad (5)$$

where e is elementary charge, p_σ is conductivity spin asymmetry, p_N is the asymmetry of the spin population, λ_N (λ_F) is the spin diffusion length of NM (FM), θ_N (θ_F) is the SHA of NM (FM), and ε_F is the Fermi energy of FM. The parameters used in the calculation are shown in Table 1[9),10),23),24)]. In the calculation of Fig. 4(b), θ_F was set to zero, i.e., SI-USMR was neglected. Although the α_{USMR} / I_{ac} plotted as function of t_F assuming θ_N = −0.1 is the closest to the experimental results, the modulation of α_{USMR} / I_{ac} with respect to t_F is too weak. For example, the experimental results at $t_F \leqq 5$ nm and t_F = 17.5 nm strongly deviate from the calculation result. Therefore, we concluded that a theoretical model that does not consider SI-USMR cannot explain the thickness dependence of USMR in Ta/Co bilayer systems.

4.3 Analysis considering self-induced unidirectional spin Hall magnetoresistance

Figure 4 (c) shows the thickness evolution of α_{USMR} / I_{ac} using Eq. (5) with θ_F = 0.05, i.e., SI-USMR originating from SHE in Co is considered. The calculation result considering SI-USMR showed a stronger modulation of α_{USMR} with respect to t_F and nicely explains the experimental results when θ_N was set to −0.2. Indeed, θ_F = 0.05 and θ_N = −0.2 were consistent with previous works. θ_F of Co was estimated to be +0.1 with the spin valve method[16)] and +0.05 with our SOT measurement[20)], whereas the θ_N of Ta has been reported to be −0.1~−0.2 in previous works[23),25)]. Note that our Ta film has σ_N = 4.3 × 10^5 $(\Omega m)^{-1}$, which corresponds to the value of beta Ta having a large θ_N[26),27)]. All these facts demonstrate the consistency of our conclusion that SI-USMR exists in Ta/Co bilayer systems.

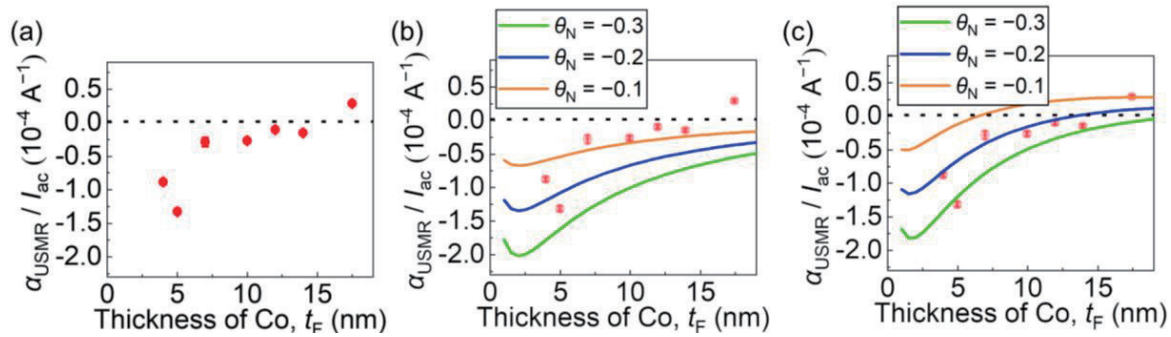

Fig. 4 (a) α_{USMR} / I_{ac} as function of t_F for Ta(5 nm)/Co (t_F nm) bilayer system. (b) α_{USMR} / I_{ac} as function of t_F calculated by solving spin-diffusion equation with different values of θ_N when θ_F was set at 0 and (c) 0.05. Experimental data is also shown as red dots as reference.

Table 1 Parameters used in calculation of thickness dependence of USMR using Eq. (5).

Parameters	p_σ	p_N	λ_F (nm)	λ_N (nm)	σ_F $(\Omega m)^{-1}$	σ_N $(\Omega m)^{-1}$	ε_F (eV)
	0.5	0	18	1.8	1.0×10^6	4.3×10^5	0.5

4.4 Comparison of self-induced spin-orbit torque and unidirectional spin Hall magnetoresistance

Finally, we compare the SI-USMR observed in this research and the SI-SOT observed in our previous research[20]. One might think that it is obvious that SI-USMR is present in a NM/FM bilayer system in the same manner as SI-SOT. However, there are two notable differences between SI-USMR and SI-SOT.

First, the relaxation mechanism of the spin current in the FM layer is different. In the case of USMR, spin relaxation is dominated by the longitudinal spin diffusion length[28] because USMR is induced by the projection of spin to the axis parallel to magnetization[8),9)]. In the case of SOT, spin relaxation is dominated by the transverse spin diffusion length[29)–31)], which is much shorter than the longitudinal spin diffusion length because SOT is induced by the projection of spin to the axis perpendicular to magnetization[20),32)].

Second, not only SHE but also the spin anomalous Hall effect (SAHE) contributes to SI-USMR. In a FM, in addition to SHE, where injected spin-polarization is parallel or anti-parallel to $\boldsymbol{J}_{c(F)} \times \boldsymbol{J}_{s(F)}$ irrespective of the magnetization direction, SAHE also generates a spin current, where spin polarization is parallel or anti-parallel to magnetization[18),33)]. Although the spin current generated by SAHE does not produce torque on magnetization, it causes the spin polarization to fluctuate, which is parallel or anti-parallel to magnetization, resulting in USMR.

In our previous work, we found that SI-SOT significantly affects the SOT measurements in Ta/Co bilayer systems, where the sign of the net SOT reverses at around $t_F = 10$ nm due to SI-SOT originating from SHE in Co[20]. On the other hand, a sign of α_{USMR} / I_{ac} is still negative up to $t_F = 14$ nm, indicating that the thickness evolution of SI-USMR is more gradual than that of SI-SOT. This is consistent with the fact that the longitudinal spin diffusion length (> 10 nm)[9),28)] that dominates SI-USMR is longer than the transverse spin diffusion length that dominates SI-SOT (< 5 nm)[19),30)].

Regarding the estimated value of θ_F, it is estimated to be ~ 0.05 in both SI-USMR and SI-SOT measurements[20)], meaning that SAHE that contributes only to SI-USMR is less significant than SHE that contributes to both SI-USMR and SI-SOT. Indeed, theoretical work has revealed that SHE is large in hcp-Co[18)]. In addition, previous experiments on anomalous SOT have shown that torque efficiency is much larger than the value expected only from anomalous Hall conductivity[19)], i.e., SHE is much larger than the anomalous Hall effect in Co. Both works suggest that SHE is dominant over SAHE in Co, consistent with our result.

5. Conclusion

In conclusion, we measured the thickness dependence of USMR in a Ta/Co bilayer system by measuring longitudinal and transverse second harmonic signals as a function of the magnetic field angle. USMR showed a negative sign when the Co film was relatively thin; however, its magnitude was strongly suppressed by increasing the thickness of the Co layer because of the cancellation of USMR originating from the SHE in Ta by SI-USMR originating from the SHE in Co. A theoretical model calculated by a spin diffusion equation that considers the SHE in Co relatively well-reproduced the thickness evolution of USMR in Ta/Co systems. A comparison between SI-USMR and the SI-SOT in our previous work revealed that the longitudinal spin diffusion length is much longer than the transverse spin diffusion length and that SHE is dominant over SAHE in Co, both of which are consistent with previous works. Our research will contribute to a better understanding of the self-induced phenomena in NM/FM bilayer systems induced by charge-to-spin conversion in the FM layer.

Acknowledgements M. A. appreciates the support from the JSPS Research Fellowship (Grant No. 22J21776).

References

1) W. Thomson: *Proc. R. Soc. London*, **8**, 546 (1856).
2) X. Wang, Y. Du, S. Dou, and C. Zhang: *Phys. Rev. Lett.*, **108**, 266806 (2012).
3) X. Dai, Z. Z. Du, and H.-Z. Lu: *Phys. Rev. Lett.*, **119**, 166601 (2017).
4) X. Huang, L. Zhao, Y. Long, P. Wang, D. Chen, Z. Yang, H. Liang, M. Xue, H. Weng, Z. Fang, X. Dai, and G. Chen: *Phys. Rev. X*, **5**, 031023 (2015).
5) E. McCann, K. Kechedzhi, V. I. Fal'ko, H. Suzuura, T. Ando, and B. L. Altshuler: *Phys. Rev. Lett.*, **97**, 146805 (2006).
6) L. Leiva, S. Granville, Y. Zhang, S. Dushenko, E. Shigematsu, R. Ohshima, Y. Ando, and M. Shiraishi: *Phys. Rev. Mater.*, **6**, 064201 (2022).
7) C. O. Avci, K. Garello, A. Ghosh, M. Gabureac, S. F. Alvarado, and P. Gambardella: *Nat. Phys.*, **11**, 570 (2015).
8) S. S. L. Zhang and G. Vignale: *Phys. Rev. B*, **94**, 140411 (2016).
9) Y. Yin, D.-S. Han, M. C. H. de Jong, R. Lavrijsen, R. A. Duine, H. J. M. Swagten, and B. Koopmans: *Appl. Phys. Lett.*, **111**, 232405 (2017).
10) C. O. Avci, J. Mendil, G. S. D. Beach, and P. Gambardella: *Phys. Rev. Lett.*, **121**, 087207 (2018).
11) M. Aoki, E. Shigematsu, R. Ohshima, T. Shinjo, M. Shiraishi, and Y. Ando: *Phys. Rev. B*, **104**, 094401 (2021).
12) M. Mehraeen and S. S. L. Zhang: *Phys. Rev. B*, **105**, 184423 (2022).
13) J. E. Hirsch: *Phys. Rev. Lett.*, **83**, 1834 (1999).
14) Y. Lv, J. Kally, D. Zhang, J. S. Lee, M. Jamali, N. Samarth, and J.-P. Wang: *Nat. Commun.*, **9**, 111 (2018).
15) S. Iihama, T. Taniguchi, K. Yakushiji, A. Fukushima, Y. Shiota, S. Tsunegi, R. Hiramatsu, S. Yuasa, Y. Suzuki, and H. Kubota: *Nat. Electron.*, **1**, 120 (2018).
16) Y. Omori, E. Sagasta, Y. Niimi, M. Gradhand, L. E. Hueso, F. Casanova, and Y. Otani: *Phys. Rev. B*, **99**, 014403 (2019).
17) A. Manchon, J. Železný, I. M. Miron, T. Jungwirth, J. Sinova, A. Thiaville, K. Garello, and P. Gambardella: *Rev. Mod. Phys.*, **91**, 035004 (2019).
18) V. P. Amin, J. Li, M. D. Stiles, and P. M. Haney: *Phys. Rev. B*, **99**, 220405 (2019).
19) W. Wang, T. Wang, V. P. Amin, Y. Wang, A. Radhakrishnan, A. Davidson, S. R. Allen, T. J. Silva, H. Ohldag, D. Balzar, B. L. Zink, P. M. Haney, J. Q. Xiao, D. G. Cahill, V. O. Lorenz, and X. Fan: *Nat. Nanotechnol.*, **14**, 819 (2019).
20) M. Aoki, E. Shigematsu, R. Ohshima, T. Shinjo, M. Shiraishi, and Y. Ando: *Phys. Rev. B*, **106**, 174418 (2022).
21) C. O. Avci, K. Garello, M. Gabureac, A. Ghosh, A.

Fuhrer, S. F. Alvarado, and P. Gambardella: *Phys. Rev. B*, **90**, 224427 (2014).
22) N. Roschewsky, E. S. Walker, P. Gowtham, S. Muschinske, F. Hellman, S. R. Bank, and S. Salahuddin: *Phys. Rev. B*, **99**, 195103 (2019).
23) L. Liu, C.-F. Pai, Y. Li, H. W. Tseng, D. C. Ralph, and R. A. Buhrman: *Science*, **336**, 555 (2012).
24) C. Hahn, G. de Loubens, O. Klein, M. Viret, V. V. Naletov, and J. Ben Youssef: *Phys. Rev. B*, **87**, 174417 (2013).
25) Q. Hao and G. Xiao: *Phys. Rev. B*, **91**, 224413 (2015).
26) N. Schwartz, W. A. Reed, P. Polash, and M. H. Read: *Thin Solid Films*, **14**, 333 (1972).
27) J. J. Colin, G. Abadias, A. Michel, and C. Jaouen: *Acta Mater.*, **126**, 481 (2017).
28) J. Bass and W. P. Pratt: *J. Phys. Condens. Matter*, **19**, 183201 (2007).
29) T. Taniguchi, S. Yakata, H. Imamura, and Y. Ando: *IEEE Trans. Magn.*, **44**, 2636 (2008).
30) A. Ghosh, S. Auffret, U. Ebels, and W. E. Bailey: *Phys. Rev. Lett.*, **109**, 127202 (2012).
31) Y. Lim, B. Khodadadi, J.-F. Li, D. Viehland, A. Manchon, and S. Emori: *Phys. Rev. B*, **103**, 024443 (2021).
32) K.-W. Kim and K.-J. Lee: *Phys. Rev. Lett.*, **125**, 207205 (2020).
33) T. Taniguchi, J. Grollier, and M. D. Stiles: *Phys. Rev. Appl.*, **3**, 044001 (2015).

Received Oct. 11, 2023; Accepted Dec. 6, 2023

J. Magn. Soc. Jpn., **48**, 34-39 (2024) <Paper>

Domain Wall Displacement Modulation GMR Sensors with Closed-loop Current-field Feedback

K. Komuro*, D. Oshima*, and T. Kato*, **

*Department of Electronics, Graduate School of Engineering, Nagoya University, *Furo-cho, Chikusa-ku, Nagoya, 464-8603, Japan*

** Institute of Materials and Systems for Sustainability, Nagoya University, *Furo-cho, Chikusa-ku, Nagoya, 464-8603, Japan*

A novel type of giant magneto-resistance (GMR) sensor utilizing domain wall displacement (DWD) modulation and a closed-loop current-field feedback technique was investigated. In this paper, a $Ni_{80}Fe_{20}$ free layer was used for the GMR sensor since the uniaxial anisotropy of $Ni_{80}Fe_{20}$ is smaller than that of the $(Co_{90}Fe_{10})_{92}B_8$ used in the previous study, resulting in a larger wall displacement with a smaller field. When the domain wall was modulated by a modulation field H_{mod} = 94 μT_{rms}, the sensitivity of the sensor increased to 2.6 mV/μT in open-loop mode compared with a sensitivity of 0.98 mV/μT for the sensor without H_{mod}. Moreover, a significant improvement in the linearity of the output was obtained by operating the DWD GMR sensor in closed-loop mode, and the sensitivity was also increased up to 4.2 mV/μT. The improvement in linearity is considered to be due to the suppression of the displacement of the average position of the domain walls by the current-field feedback. The noise floor of the output of the DWD GMR sensor under closed-loop operation was estimated to be 300 pT/Hz$^{1/2}$ at 10 Hz.

Keywords: magnetic sensors, domain wall displacement modulation, current field feedback, GMR

1. Introduction

Magneto-resistance (MR) sensors have been widely used in many applications, since they are simple two-terminal resistance devices and are easily micro-fabricated by low cost lithography techniques. Major applications of the MR sensors are hard-disk-drive (HDD) heads[1)-3)], linear-rotary position encoders[4),5)], and recently they are reported to be applied to bio-magnetic sensors[6),7)] and automotive current monitors[8)] by improving their sensitivity and linearity, respectively. In order to improve the sensitivity of the MR sensors, tunnel magneto-resistance (TMR) sensors with high magnetoresistance (MR) ratio over 100% are typically utilized. For example, sub-pT field[9)] detection using TMR sensor was reported for the applications to magneto-cardiography (MCG)[10)] and magneto-encephalography (MEG)[11)] at room temperature. However, the TMR sensors consist of magnetic tunnel junctions (MTJ) and basically have a large resistance, resulting in the larger shot noise than that of a giant magnetoresistance (GMR) sensors[12)]. The GMR sensors have a small resistance due to their metallic nature and high signal-to-noise (S/N) ratio at low frequencies. Moreover, the fabrication process of GMR sensors is simple compared to TMR sensors, which is an apparent advantage in terms of industrial applications. Recently, several studies on GMR sensors report to detect magnetic field as small as pT. For example, an antiphase modulation bridge detection technique utilizing GMR elements with symmetric response was reported in Ref. 13. This technique reduces 1/*f* noise significantly which mainly dominates the noise spectrum of GMR elements at frequency f < 100 kHz. We have also studied the antiphase modulation GMR sensors and reported that the non-linearity due to the hysteresis in the free layers and the temperature drift are significantly improved[14)] by introducing a closed-loop current-field feedback technique[15)]. However, the sensor output was insufficient to detect pT-level field.

One of the ways to improve the sensor output is to use magnetic flux concentrators (MFC) to amplify the magnetic field applied to the GMR elements[16)]. For instance, Kikitsu *et al.* reported the detectivity of 13 pT/Hz$^{1/2}$ at 100 Hz in antiphase modulation GMR sensors by using MFCs[17)]. Moreover, Tatsuoka *et al.* utilized the GMR sensors with MFCs as well as the compensating coils wounded around the MFCs, and high detectivity and wide dynamic range were reported[18)]. Another way is to detect the field along the easy axis of GMR sensors since the magnetic susceptibility along the easy axis is much higher than that along the hard axis. Conventional MR sensors detect the fields along the hard axis due to the small hysteresis. We have previously reported domain wall displacing (DWD) GMR sensors to detect the fields along the easy axis, which results in several-times increase of the sensor output and enables to detect nT level magnetic fields[19)-21)]. Liao *et al.* and Huang *et al.* also reported that DWD modulation effectively reduces the hysteresis and increases the sensitivity compared to no modulation[22), 23)]. However, because DWD involves the motion of the domain walls, the sensor output still has small hysteresis and contains Barkhausen noise.

In this study, we introduced the closed-loop current-field feedback technique to DWD modulation GMR sensors to solve these issues. Here, we discuss the basic operation and performance of the closed-loop DWD modulation GMR sensor, and report the detectivity of the present closed-loop DWD modulation GMR sensor. MFC

Corresponding author: T. Kato
(e-mail: kato.takeshi.i6@f.mail.nagoya-u.ac.jp).

is expected to be applied to the present sensor for further improvement of the detectivity which will be studied in future work.

2. Operating principle

2.1 Domain wall modulation

Figures 1 and 2 show the circuit diagram of DWD GMR sensor and the schematic of a GMR sensor with an Al wire to apply modulation and feedback fields, respectively. As shown in Fig. 1, a GMR element was connected to the bridge circuit and the modulation field H_{mod} was applied along the easy axis by flowing the current through the Al wire placed upon the GMR element (see Fig. 2). Here we assume the stripe domains in the free layers as shown in the illustration of Fig. 3 due to the energy balance between induced anisotropy of the free layer and the shape anisotropy of the GMR wire. The DWD modulation field H_{mod} at the frequency f_{mod} of 100 kHz modulates the position of the domain walls as in Fig. 3. f_{mod} is much higher than the frequency of detecting fields H_{ext}. Since the domain walls are oscillated by H_{mod}, the center positions of the domain wall shift sensitively to H_{ext} which is smaller than the wall coercivity. This technique is considered to be effective to reduce the well-known Barkhausen effect[20] and enhance the sensitivities[22), 23)].

The bridge circuit output is proportional to the ratio of the parallel and antiparallel domain areas to the reference layer of the GMR element. Both H_{mod} and H_{ext} components appear in the instrumentation amplifier (IA) output, since both fields affect the domain area, and H_{mod} component was filtered by the low pass filter (LPF).

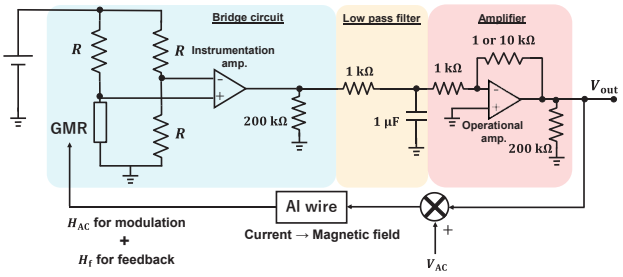

Fig. 1 Circuit diagram of the proposed GMR sensor using domain wall displacement (DWD) modulation with closed-loop current-field feedback.

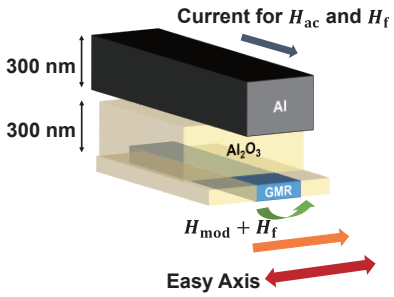

Fig. 2 Schematic of GMR sensor device with GMR element and Al wire. Easy axis of GMR element is parallel to wire width direction. Modulation field H_{mod} and feedback field H_{f} are produced by current flowing through Al wire.

2.2 Current field feedback

The output V_{out} in Fig. 1 is used to flow the current in Al wire shown in Fig. 2 to produce the feedback field H_{f} which cancels H_{ext}. Therefore, the relation between V_{out} and H_{ext} is expressed as following equation:

$$V_{\mathrm{out}} = \frac{1}{\frac{1}{K_{\mathrm{H\to V}} \cdot G_{\mathrm{IA}} \cdot G_{OA}} + F} H_{\mathrm{ext}}, \tag{1}$$

where $K_{\mathrm{H\to V}}$ is the conversion constant from field to voltage, and G_{IA} and G_{OA} are the gains of IA and the following operational amplifier (OA) (see Fig. 1). F stands for the feedback constant determined by the width of the Al wire and the resistance connected in series to

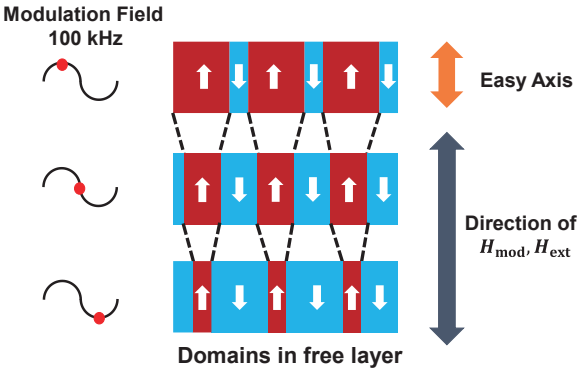

Fig. 3 Illustration of domain wall displacement (DWD) modulation. Domain walls in free layer oscillate due to modulation field H_{mod} at frequency f_{mod} of 100 kHz. H_{mod} and detected field H_{ext} are applied along easy axis of free layer.

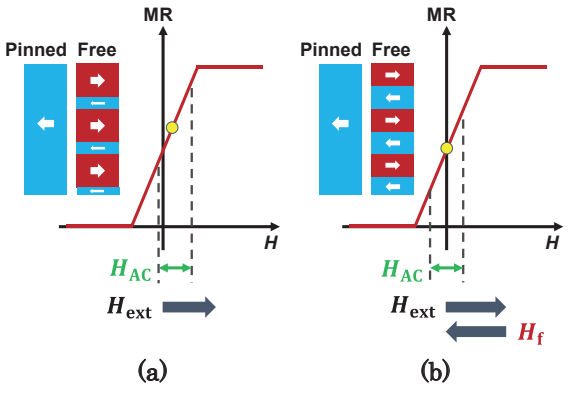

Fig. 4 Illustrations of the operation point under (a) open-mode and (b) closed-loop mode of DWD GMR element. Insets show the time averaged domain structure of the free and the pinned layers, where red and blue are domains parallel and antiparallel to the reference layer, respectively.

the Al wire. If $1/(K_{H\to V}\cdot G_{IA}\cdot G_{OA}) \ll F$, V_{out} can be determined only by F. In other words, the feedback current can be adjusted by tuning the loop gain which is the product of G_{IA} and G_{OA}.

Figure 4 shows the schematic of the current-field feedback operation of the DWD GMR sensor. When no H_{ext} is applied, the time average of the areal ratio of domains between antiparallel (red) and parallel (blue) to the pinned layer is assumed to be 1:1. If H_{ext} is applied to the GMR element without the feedback circuit, which is referred to as "open mode", the center positions of the domain walls shift due to H_{ext} (see Fig. 4 (a)). On the other hand, closed-loop current-field H_f cancels H_{ext} in the closed-loop mode (see Fig. 4 (b)), which suppresses the shift of domain walls under H_{ext}.

3. Experimental setup

3.1 GMR stacks

GMR stacks were fabricated by 8-cathodes RF magnetron sputtering system. The stacks were substrate / Ta (5) / $Ni_{80}Fe_{20}$ or $(Co_{90}Fe_{10})_{92}B_8$ (10) / Cu (4) / $Co_{90}Fe_{10}$ (3) / $Mn_{80}Ir_{20}$ (8) / Ta (3) and substrate / Ta (5) / $(Co_{90}Fe_{10})_{92}B_8$ (10) / Cu (2.2) / $Co_{90}Fe_{10}$ (3) / $Mn_{80}Ir_{20}$ (8) / Ta (3), where the numbers in parentheses indicate the thickness in nanometer. The latter is the same stack as studied in Ref. 19-21. The substrate was Si substrate with the 500 nm-thick thermally oxidized layer. During the deposition, the external field of 27mT was applied to induce the exchange bias in the reference layer and the uniaxial anisotropy in the free layer.

3.2 Microfabrication

GMR stacks were microfabricated as shown in Fig. 2. First, the GMR films were structured with the size of 30 μm × 300 μm by maskless lithography followed by Ar^+ ion milling. Ar^+ ions were produced by the Kaufman-type Ar^+ ion source and were incident on the sample with an angle of 90° from the surface. The incident ion energy was set at 700 eV. Then, Al_2O_3 insulator with the thickness of 300 nm was deposited. Finally, Al wires with the size of 60 μm × 360 μm and the thickness of 300 nm were fabricated above the GMR elements using a lift-off technique.

After the microfabrication, the GMR sensors with $Ni_{80}Fe_{20}$ free layer were annealed in vacuum at 270°C for 10 minutes under the field of 230 mT. The field was applied along the short axis of the GMR elements. The annealing temperature was set at 270°C, since the blocking temperature of the IrMn is 270℃, and Mn atoms start to diffuse into the adjacent layers above this temperature[24), 25)]. The GMR sensors with $(Co_{90}Fe_{10})_{92}B_8$ free layer were not annealed, since the annealing would crystallize the free layer, which increases the coercivity.

3.3 Measurement setup

The GMR sensor devices were connected in the bridge circuit as shown in Fig. 1 and placed into the measurement system with a pair of coils. The pair of coils produces H_{ext}. H_{ext} was used as an input of the DWD GMR sensor as well as to measure the MR loops of the GMR elements. Parameters of the circuit are indicated in Table 1. Hereafter, we call three types of the circuit modes as "Open-1"," Closed-1" and "Closed-10". "Open-1" indicates that the sensor is operated under open mode and the OA gain is $G_{OA}=1$, corresponding to the conventional DWD GMR sensors[19)-21)]. "Closed-1" and "Closed-10" indicate that the sensor is operated under closed-loop current-field feedback with the OA gains of $G_{OA}=1$ and $G_{OA}=10$, respectively.

Table 1 Parameters of measurement circuit.

Parameter	Value
Voltage of bridge circuit: V_B	3 V
Frequency of H_{mod}: f_{mod}	100 kHz
Gain of IA: G_{IA}	456
Cut off frequency of LPF	159.2 Hz
Gain of OA: G_{OA}	1 (Open-1, Closed-1) 10 (Closed-10)

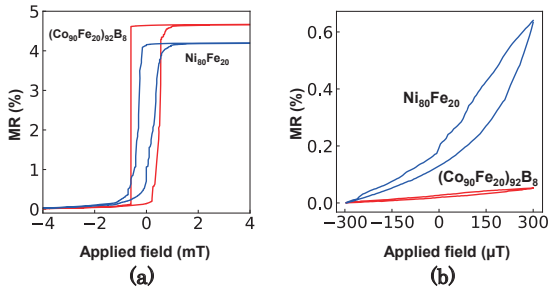

Fig. 5 MR loops of GMR elements with $Ni_{80}Fe_{20}$ (blue) and $(Co_{90}Fe_{10})_{92}B_8$ (red) free layers with field sweep ranges of (a) -4 mT $\le H_{ext} \le 4$ mT and (b) -300 μT $\le H_{ext} \le 300$ μT.

4. Results and Discussions

4.1 MR properties

Figure 5 shows the MR loops of GMR elements with $Ni_{80}Fe_{20}$ and $(Co_{90}Fe_{10})_{92}B_8$ free layers with the field sweep ranges of (a) $|H_{ext}| \le 4$ mT and (b) $|H_{ext}| \le 300$ μT. From Fig. 5 (a), MR ratio and coercivity of the GMR with $Ni_{80}Fe_{20}$ are smaller than those with $(Co_{90}Fe_{10})_{92}B_8$. The smaller MR ratio in GMR with $Ni_{80}Fe_{20}$ is owing to the thicker spacer layer between the free and reference layers. On the other hand, for smaller sweep field of $|H_{ext}| \le 300$ μT shown in Fig.5 (b), the GMR with $Ni_{80}Fe_{20}$ free layer exhibited large MR change over 0.6 % while the one with $(Co_{90}Fe_{10})_{92}B_8$ was only 0.05%. This is due to the large coercivity of $(Co_{90}Fe_{10})_{92}B_8$, and thus, $Ni_{80}Fe_{20}$ free layer is preferable to obtain higher output within the small field range.

4.2 Domain wall modulation

Since a sinusoidal H_{mod} with the frequency of 100 kHz modulates the domain walls in the free layer, the modulated signal can be observed in the output of IA.

Figure 6 shows the IA output when H_{mod} of 94μT$_{rms}$ at the frequency of 100 kHz was applied, where no H_{ext} was applied. it was slightly distorted due to the hysteresis of the MR curves. The amplitude of the waveform was not varied drastically when the external field H_{ext} in the range of ±100μT was applied.

4.2 H_{mod} Dependence of sensitivity and non-linearity

Figure 7 shows H_{ext}-V_{out} properties of the DWD GMR sensor with $Ni_{80}Fe_{20}$ free layer under Open-1 mode, where H_{mod} was (a) 0, (b) 37.6, and (c) 94.0 μT$_{rms}$. Blue solid curves indicate the measured data. The measured data were fitted with Rayleigh loops expressed as follows, since the output properties reflect the minor loop of $Ni_{80}Fe_{20}$ free layer.

$$V_{out} = \begin{cases} -aH_{ext}^2 + bH_{ext} + c \\ aH_{ext}^2 + bH_{ext} - c \end{cases} \quad (2)$$

The fitted Rayleigh loops are shown as the red dashed lines in the figure. For the fitting, b was first estimated from two loop ends, then a and c were estimated by the least square fit. In this paper, we define the non-linearity of sensor output as a normalized by the full scale of the sensor output V_{full}, and the sensitivity of the sensor was defined as the absolute value of b.

Figure 8 show (a) sensitivity $|b|$ and (b) non-linearity a/V_{full} of DWD GMR sensor with $Ni_{80}Fe_{20}$ free layer as a function of H_{mod}. Both sensitivity and non-linearity increased with increasing H_{mod} as discussed in Fig. 7. Dependence of sensitivity and non-linearity for Closed-1 and Closed-10 modes will be discussed later.

In order to discuss the reason of the increases of sensitivity and non-linearity with H_{mod}, domain structures of the free layer were observed with the Kerr microscope. For the measurement, we deposited the samples with a stack of substrate / NiFe (10) / SiN (40) and microfabricated in the same size as GMR elements of the sensor devices. Before the observation, the sample was magnetically saturated with a field of 6 Oe. Figure 9 shows the Kerr microscope images of $Ni_{80}Fe_{20}$ rectangle at fields of (a) 0 Oe and (b) 1 Oe. At 0 Oe, the flux-closure domains were observed. The area of domains parallel to the external field was confirmed to increase at 1 Oe as shown in Fig. 9 (b), and flux-closure domain structure is partially collapsed by the large displacement of the domain walls. The domain structure was completely different from the stripe domains of $(Co_{90}Fe_{10})_{92}B_8$ thin films reported in Ref. 21 (see Fig. 9 (c)).

From the domain observations, we consider the reason of enhancement in the hysteresis of the output under the large modulation field (see Fig. 7) is due to the variation

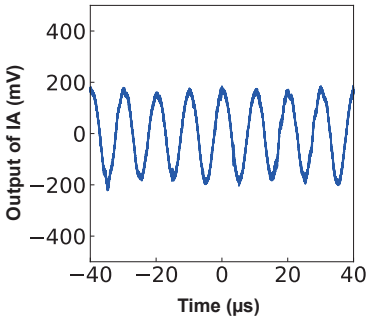

Fig. 6 IA output waveform of DWD GMR sensor with $Ni_{80}Fe_{20}$ free layer when H_{mod} of 94μTrms at the frequency of 100 kHz and no external field H_{ext} were applied.

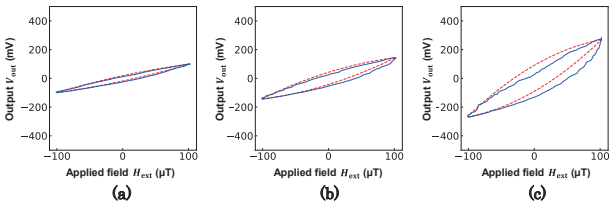

Fig. 7 H_{ext}-V_{out} properties of DWD GMR sensor with $Ni_{80}Fe_{20}$ free layer under Open-1 mode applying (a) H_{mod} = 0 μT$_{rms}$, (b) H_{mod} = 37.6 μT$_{rms}$, (c) H_{mod} = 94.0 μT$_{rms}$. Solid blue curves indicate measured data, and red dashed curves are fitted data with Rayleigh loops expressed in Eq. (2).

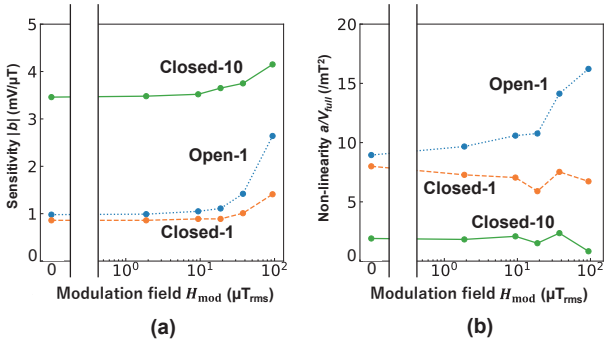

Fig. 8 (a) Sensitivity and (b) non-linearity of DWD GMR sensor with $Ni_{80}Fe_{20}$ free layer as function of H_{mod}. Blue circles are for Open-1 mode, orange circles are for Closed-1 mode, and green circles are for Closed-10 mode.

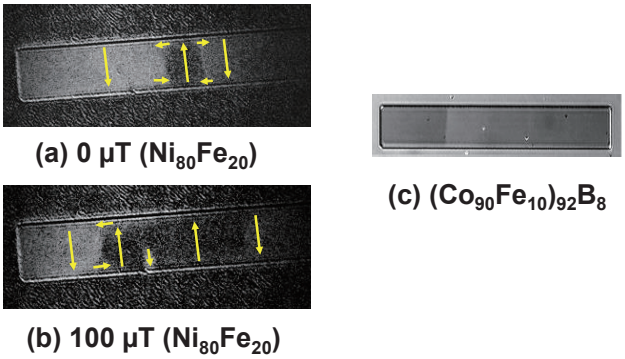

Fig. 9 Kerr microscope images of $Ni_{80}Fe_{20}$ element under external fields of (a) 0 μT and (b) 100 μT. (c) Domain structure of CoFeB is also shown as reference[21].

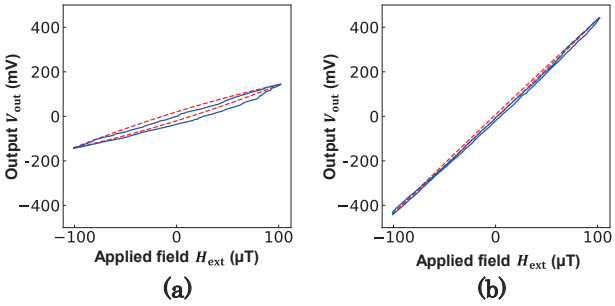

Fig. 10 H_{ext}-V_{out} properties of DWD GMR sensor with $Ni_{80}Fe_{20}$ free layer under (a) Closed-1 and (b) Closed-10 modes. Solid blue curves indicate measured data, and dashed red curves are fitted with Rayleigh loops in Eq. (2).

of the domain structures under the fields. The increase of the sensitivity with H_{mod} is considered to be due to the reduction of wall coercivity under H_{mod} as discussed in the previous paper[21].

4.3 Effect of feedback operation

Figure 10 shows H_{ext}-V_{out} profiles of DWD GMR sensor under (a) Closed-1 and (b) Closed-10 modes. H_{mod} was fixed at 94.0 μT_{rms}. The normalized a was 6.73 mT^{-2} for Closed-1, and 0.83 mT^{-2} in Closed-10 mode. From these results, the non-linearity was confirmed to be drastically improved by applying a current-field feedback technique as well as the increase of gain G_{OA}. Compared to the Open-1 mode as shown in Fig. 6 (c), 95% decrease of the non-linearity was confirmed in Closed-10 mode.

4.4 Summary of sensitivity and non-linearity

Figures 8 (a) and (b) summarize the sensitivity and the non-linearity as a function of H_{mod} under three operation modes, Open-1, Closed-1, and Closed-10. As shown in Fig. 8 (a), sensitivity increased with increasing H_{mod} because of the reduction of wall coercivity by H_{mod}. Moreover, the sensitivity for Closed-10 mode was much larger than that for Closed-1 mode. This is due to the increase of $K_{H\to V} \cdot G_{IA} \cdot G_{OA}$ in equation (1).

As shown in Fig. 8 (b), non-linearity decreased in order of Open-1, Closed-1, Closed-10 at any H_{mod}. Therefore, we can conclude that closed-loop feedback operation is effective to improve the linearity of the DWD GMR sensors.

In order to discuss the improvement of linearity, the effective field applied to the GMR elements were estimated in each mode. Effective input field H_{eff} is expressed as follows:

$$H_{eff} = H_{ext} - FV_{out} = \frac{1}{1 + \frac{K_{H\to V} \cdot G_{IA} \cdot G_{OA}}{F}} H_{ext} = \eta H_{ext} \quad (3)$$

Here, $K_{H\to V}$ were calculated from $|b|$ for Open-1 mode,

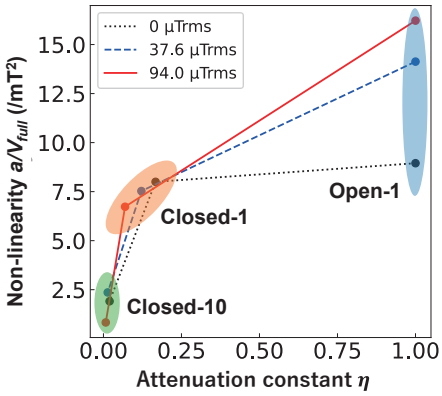

Fig. 11 Relations of derived η and non-linearity (normalized a). Red circles are for H_{mod} = 94.0 μT_{rms}, blue circles are for H_{mod} = 37.6 μT_{rms}, and black circles are for H_{mod} = 0. Circuit modes are also indicated in figure.

and the relation between η and the normalized a were evaluated for every H_{mod}. Note that η means the attenuation constant of the field applied to the GMR elements. The smaller η means the larger H_f to cancel H_{ext}. Figure 11 shows η dependence of the normalized a of DWD GMR sensors under different operation modes. Open-1 mode has η of 1 independent of H_{mod}, since $F = \infty$ in Eq. (3). According to the results, the normalized a decreased with decreasing η. The reduction of η will impedes the displacement of the average positions of the domain walls under DWD modulation, which is considered to be effective to reduce non-linearity of the sensor output. In Closed-10 mode, the displacement of the average position of the domain wall is negligibly small in the range of the total applied field ±100 μT., resulting in the significant improvement of output linearity.

4.5 Noise spectrum

Noise spectrum of V_{out} of DWD GMR sensor with $Ni_{80}Fe_{20}$ free layer under Closed-10 mode was measured. H_{mod} was 94.0 μT_{rms}. The whole sensor circuit was placed inside the NiFe magnetic shield box (Ohtama) with a shielding factor of 66 dB, and the terminal of V_{out} was connected to the high pass filter with cut-off frequency of 0.1 Hz (NF Dual Programmable Filter 3624). The noise spectrum was measured by the FFT analyzer (ONOSOKKI FFT Analyzer CF-9200).

Figure 12 shows the FFT spectrum of V_{out}, where the vertical axis was converted to the input referred magnetic field. From the spectrum, the noise floor at 10 Hz was estimated to be 300 $pT/Hz^{1/2}$ as shown in the red line in the figure. Further reduction of the noise floor is expected by applying MFC which will be studied in future work.

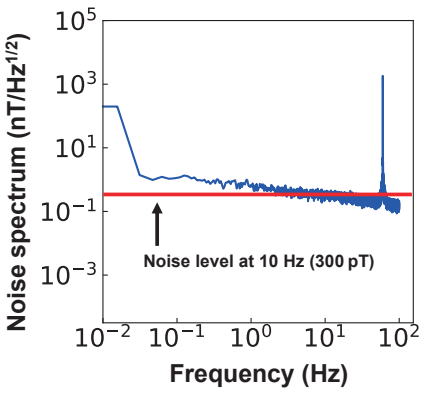

Fig. 12 FFT spectrum of output of DWD GMR sensor under closed-loop operation with OA gain G_{OA} of 10. H_{mod} of 94 μT_{rms} was applied during measurement, and no external field H_{ext} was applied.

5. Conclusion

In this paper, the closed-loop current-field feedback operation was implemented to the DWD GMR sensors. $Ni_{80}Fe_{20}$ were used for the free layer since the uniaxial anisotropy is smaller than that of $(Co_{90}Fe_{10})_{92}B_8$ used in the previous study, resulting in larger wall displacement in smaller applied field. By applying H_{mod} to DWD GMR sensor under open mode operation, the sensitivity was increased roughly twice compared to GMR sensor without H_{mod}. Hysteresis (non-linearity) of the output also increased with increasing H_{mod} due to the displacement of the average positions of the domain walls. However, the large hysteresis of DWD GMR sensor with $Ni_{80}Fe_{20}$ free layer under open mode operation significantly reduced by applying closed-loop current-field feedback operation. The feedback operation with large loop gain effectively impedes the displacement of the average positions of the domain walls, resulting in the reduction of non-linearity of V_{out}. Finally, the noise floor of 300 $pT/Hz^{1/2}$ was obtained for DWD GMR sensor under the closed-loop mode. Further increase of the sensitivity is expected by applying MFCs, and from these results, the proposed sensor was confirmed to be one of the potential candidates of high sensitivity GMR sensors.

Acknowledgments We would like to thank Prof. T. Uchiyama, Nagoya University for helping to measure the noise spectrum of the sensor output. This work is supported in part by JSPS KAKENHI Grant Number 20H02182. This work was also supported in part by the Project of Creation of Life Innovation Materials for Interdisciplinary and International Researcher Development of the Ministry of Education, Culture, Sports, Science and Technology (MEXT), Japan. A part of this work was performed under the Research Program of "Dynamic Alliance for Open Innovation Bridging Human, Environment and Materials" in Network Joint Research Center for Materials and Devices. A part of this work was conducted at the Next-generation biomaterials Hub, Nagoya University, supported by Advanced Research Infrastructure for Materials and Nanotechnology in Japan of MEXT, Japan.

References

1) R. Rottmayer and J.-G. Zhu: *IEEE Trans. Magn.*, **31**, 2597 (1995).
2) T. Miyazaki and N. Tezuka: *J. Magn. Magn. Mater.*, **139**, 231 (1995).
3) S. Mao: *IEEE Trans. Magn.*, **42**, 97 (2006)
4) H. A. M. van den Berg et al.: *J. Magn. Magn. Mater.*, **165**, 524 (1997)
5) C. Giebeler, D. J. Adelerhof, A. E. T. Kuiper, J. B. A. van Zon, D. Oelgeschläger, and G. Schulz: *Sens. Actuators A Phys.*, **91**, 16 (2001).
6) G. Li et al.: *J. Appl. Phys.*, **93**, 7557 (2003)
7) M. Pannetier-Lecoeur, H. Polovy, N. Sergeeva-Chollet, G. Cannies, C. Fermon, and L. Parkkonen: *J. Phys. Conf. Ser.*, **303**, 012054 (2011).
8) X. Liu, C. Zheng, C. Liu, and P. W. T. Pong: *IEEE Sens. J.*, **18**, 3098 (2018).
9) M. Oogane *et al.*: *Appl. Phys. Express*, **14**, 123002 (2021).
10) K. Fujiwara *et al.*: *Appl. Phys. Express*, **11**, 023001 (2018).
11) A. Kanno *et al.*: *Sci. Rep.*, **12**, 6106 (2022).
12) H. Weitensfelder, H. Brueckl, A. Satz and K. Pruegl: *Phys. Rev. Applied* , **10**, 054056 (2018).
13) S. Shirotori et.al.: *IEEE Trans. Magn.*, **57**, 4000305 (2021).
14) K. Komuro, D. Oshima and T. Kato: *IEEE Trans. Magn.*, **59**, 4000405 (2023).
15) G. A. Wang, S. Arai, T. Kato, and S. Iwata: *J. Phys. D Appl. Phys.*, **44**, 235003 (2011).
16) N. Smith, F. Jeffers, J. Freeman: *J. Appl. Phys.*, **15**, 5082 (1991).
17) A. Kikitsu et. al.: *Jpn. J. Appl. Phys.* **62**, SB1007 (2023).
18) T. Tatsuoka et. al., TechRxiv. Preprint (2023) https://doi.org/10.36227/techrxiv.22850834.v2.
19) G. A. Wang, S. Nakashima, S. Arai, T. Kato, and S. Iwata: *J. Appl. Phys.*, **107**, 09E709 (2010).
20) G. A. Wang, Y. Masuda, T. Kato, and S. Iwata: *J. Phys. D Appl. Phys.*, **43**, 455001 (2010).
21) G. A. Wang, Y. Masuda, T. Kato, and S. Iwata: *J. Appl. Phys.*, **109**, 07E523 (2011).
22) S. -H. Liao et. al.: *IEEE Trans. Magn.*, **57**, 4000204 (2021).
23) H. -S. Huang et. al.: *IEEE Trans. Magn.*, **58**, 4001004 (2022).
24) L. Wang et. al., *IEEE Sens. J.*, **21**, 27393 (2021).
25) H. Li, P. P. Freitas, Z. Wang, J. B. Sousa, P. Gogol, and J. Chapman: *J. Appl. Phys.*, **89**, 6904 (2001).

Received Oct. 26, 2023; Accepted Dec. 28, 2023

Editorial Committee Members・Paper Committee Members

Notice for Photocopying

編集委員・論文委員

複写をされる方へ

Journal of the Magnetics Society of Japan

Vol. 48 No. 2 (通巻第332号) 2024年3月1日発行

Vol. 48 No. 2 Published Mar. 1, 2024
by the Magnetics Society of Japan
Tokyo YWCA building Rm207, 1–8–11 Kanda surugadai, Chiyoda-ku, Tokyo 101–0062
Tel. +81–3–5281–0106 Fax. +81–3–5281–0107

Printed by JP Corporation Co., Ltd.
Sports Plaza building 401, 2–4–3, Shinkamata Ota-ku, Tokyo 144–0054
Advertising agency: Kagaku Gijutsu-sha

発行：(公社)日本磁気学会 101–0062 東京都千代田区神田駿河台 1–8–11 東京YWCA会館 207 号室
製作：ジェイピーシー 144–0054 東京都大田区新蒲田 2–4–3 スポーツプラザビル401 Tel.（03）6715–7915
広告取扱い：科学技術社 111–0052 東京都台東区柳橋 2–10–8 武田ビル 4F Tel.（03）5809–1132